

Structural and Kinematic Analysis of Eastern Ovda Regio, Venus: Implications for Crustal Plateau Formation

Rebecca Ghent and Vicki Hansen

Department of Geological Sciences, Southern Methodist University, Dallas, Texas 75275-0395

E-mail: rghent@mail.smu.edu

Received February 26, 1998; revised January 6, 1999

Crustal plateaus on Venus constitute one of that planet's most intriguing tectonic features. They host so-called "tessera" terrain, or deformed crust exhibiting two or more sets of intersecting tectonic lineaments, which comprises ~8% of Venus' surface. Major questions surrounding crustal plateaus and tessera terrain include: (1) What is the nature of crustal plateau deformation? What structures are present, and what are their spatial and temporal relations? (2) What is the global distribution of tessera terrain? Does it form a global layer under the regional plains, cropping out in crustal plateaus, or is it confined to crustal plateaus? and (3) What are the implications of (1) and (2) for understanding the processes responsible for formation and deformation of crustal plateaus? Structural and kinematic analyses reveal that deformation at Ovda Regio, Venus largest crustal plateau, is characterized by linear shallow steep-sided troughs (ribbons), long arcuate long-wavelength folds, short mid-wavelength folds, and wide complex graben. Temporal relations between structures lead to a three-phase regional strain history consisting of (1) layer-normal flattening of a thin competent membrane resulting in radially oriented, distributed extension (ribbon formation); (2) modest contraction of a thicker layer (concentric folding at plateau margins, interference folding in the plateau interior); and (3) limited extension localized at fold crests (graben formation). Wavelength analysis of ribbons and folds places limits on the thickness of the competent layer during each stage of deformation and reflects an early shallow brittle-ductile transition (BDT) that deepened with time. Ovda's deformation, topography, and gravity are all spatially correlated, strongly suggesting a genetic relationship between surface deformation and processes causing crustal thickening and plateau uplift. Thus tessera terrain at Ovda Regio is likely confined to the topographically high plateau and does not extend beneath the surrounding regional plains. Similar patterns persist at other crustal plateaus, indicating that tessera terrain is in general confined to crustal plateaus and does not form a globally continuous layer. Ovda's structures, their spatial and temporal relations, the resulting strain history, and the behavior of the BDT through time support a model of mantle plume upwelling in a thin lithospheric regime for crustal plateau formation and contradict previous downwelling models. Similarities between structural and kinematic trends at Ovda Regio and other crustal plateaus lend support to this idea. © 1999 Academic Press

Key Words: Ovda Regio; tessera; crustal plateaus; structure; ribbons.

INTRODUCTION

Crustal plateaus represent a major class of tectonic feature on Venus and are the focal point for a heated debate concerning venusian tectonics. Crustal plateaus are characterized by so-called "tessera terrain," originally defined as any terrain exhibiting two or more sets of intersecting lineaments (Barsukov *et al.* 1986, Basilevsky *et al.* 1986) and further characterized and subdivided into distinct types by Hansen and Willis (1996). The debate has two main positions: Do crustal plateaus represent outcrops of a global layer of tessera, or do they instead reflect localized processes that created the plateaus and also caused the surface deformation they exhibit? If the latter, then what process(es) were responsible? Any answer to this question must address crustal plateau surface structures. Structural features preserved on planetary surfaces record strain resulting from stresses in the crust or lithosphere. Thus, mapping the spatial distribution, orientations, and temporal relations between and among structures can provide clues about regional-scale deformation mechanisms and therefore provide clues for tectonic processes. This is particularly true on Venus, which lacks an asthenosphere and shows strong mechanical coupling between mantle and crust (e.g., Phillips 1990, Bindschadler and Parmentier 1990, Grimm and Phillips 1991, 1992). In this paper we present an integrative study of surface structures and their relationship to topography and gravity for the crustal plateau Ovda Regio. Our goal is to elucidate crustal plateau deformation and formation mechanisms.

Ovda Regio

Ovda Regio resides in the equatorial highland Aphrodite Terra and is Venus' largest crustal plateau (approximately 6000 × 2500 km), extending from 10°N to 15°S and from 50°E to 110°E (Fig. 1). Ovda borders regional plains to the north, the large tessera inlier Salus Tessera to the west, the crustal plateau Thetis Regio to the east, and Kuanja and Ix Chel chasmata and associated corona-like structures to the south. Fractures and other structures associated with these chasmata overlap spatially with crustal plateau structures at the plateau's southern margin. Ovda's topographic boundaries are steep, with elevations dropping from

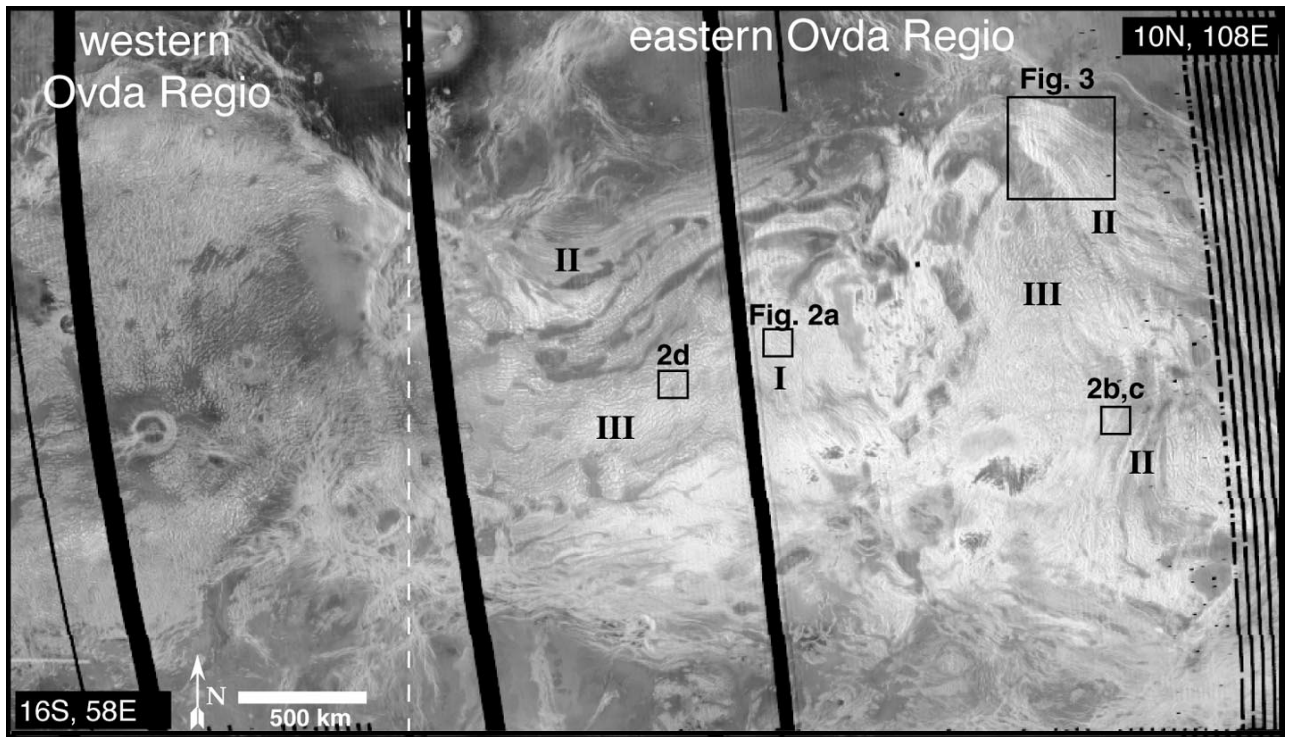


FIG. 1. Magellan SAR image of Onda Regio showing the study area, structural Domains I, II, and III and locations of Figs. 2a–2d and 3 (boxes).

4 to 5 km above mean planetary radius (MPR) in the plateau interior to elevations at or near MPR in the plains (see Bindschadler *et al.* 1992a, Fig. 11, for topographic profiles). A topographic saddle, ~ 2.5 km above MPR, lies between eastern Onda and Thetis regiones. Elevations between western Onda and Salus are near MPR. Onda is composed of two quasi-circular regions, which may represent separate tectonic entities. The western portion (herein called western Onda) extends from 10°N to 15°S and 50°E to 75°E ; the eastern portion (herein called eastern Onda) extends from 10°N to 15°S and 75°E to 110°E . This work focuses on eastern Onda.

Other Work

Bindschadler *et al.* (1992a) conducted preliminary analysis of Magellan data for Onda Regio, focusing on characterizing altimetry and gravity, accompanied by a reconnaissance study of tectonic structures along Onda's NE margin. These workers reported no formal geologic mapping or structural analysis of this area. Gilmore *et al.* (1998) mapped structures in isolated areas of Onda Regio, focusing on the sequence of deformation at each location. The current work represents the first comprehensive geologic analysis of Onda Regio.

Methodology

Magellan synthetic aperture radar (SAR) data are ideal for examining structures on Venus. Because erosion is minimal on Venus (e.g., Kaula 1990, Connors 1995) and the other processes

which could modify structures (lava flows or impact cratering) are not significant for crustal plateaus, surface morphologies reflect the underlying structural forms (Connors 1995). Therefore, this analysis relies heavily on SAR data. Magellan altimetry and gravity data are useful for determining gross plateau structure and support mechanisms, but do not have sufficient spatial resolution to address tectonic structures.

Our structural analysis employed digital full-resolution (FMIDR; 75 m/pixel) and compressed-once (C1MIDR; 225 m/pixel) Magellan SAR images, viewed on a SUN Sparc-10 workstation equipped with the Interactive Data Language (IDL) for image processing. IDL allows analysis of digital images while manipulating the grayscale stretch, greatly enhancing our ability to distinguish lineaments and surfaces, especially in areas of high radar backscatter. We also used 1 : 5,000,000 hard-copy mosaicked SAR images for synthesis of detailed maps. In conducting the structural analysis, we were concerned with two major issues: (1) radar interpretation and (2) structural methods.

Radar interpretation. The NASA Magellan mission produced high-resolution (~ 100 m) SAR images of $\sim 98\%$ of Venus' surface. The Magellan satellite used a side-looking transmitter/receiver which emitted pulsed microwave energy at a wavelength of 12.6 cm. Data were collected in both left- and right-looking geometries and from various incidence angles (Ford and Plaut 1993, Plaut 1993a). SAR images result from microwave energy reflected from the surface. The strength of a reflected pulse,

manifested as brightness in SAR images, depends primarily on surface slope and roughness (Ford *et al.* 1989, Farr 1993). A smooth slope oriented at a low local incidence angle (i.e., the angle between the surface normal and incident radar) reflects most of the incident energy back to the spacecraft, producing a brighter lineament in SAR images than a slope oriented at a high local incidence angle, which reflects most of the incident energy away from the receiver. For a given uniform slope, a surface with high meter- or sub-meter-scale roughness leads to high radar backscatter and appears brighter in SAR images than a smooth surface. Roughness at scales less than the 12.6 cm radar wavelength appears dark in SAR images. Geological features are manifested in SAR images as lineaments and surfaces; therefore radar brightness characteristics are eminently useful in identifying and characterizing structures. Features identifiable in SAR images include wrinkle ridges, folds, fractures, scarps, impact craters, and lava flow and ejecta units.

Radar images are produced by converting the two-way travel time for a reflected pulse to a ground range, assuming flat topography. Thus, topographic slopes may be subject to imaging artifacts (e.g., Farr 1993, Plaut 1993a, Cannors 1995). Slopes may be imaged as shorter or longer than they actually are (foreshortening or elongation), may be imaged with their tops below their bases (layover), or may not be imaged at all (radar shadow). Foreshortening and layover occur for slopes facing incident radar, whereas elongation and shadow affect slopes facing away from incident radar; none of these effects will affect slopes that strike parallel to the radar look direction. Layover, foreshortening, and elongation are accentuated for small radar incidence angles, and shadow is accentuated for large incidence angles. Radar incidence angles for all Magellan cycles are greatest between 10°N and 10°S (42.3–45.7° for cycle 1, 24.9° for cycle 2, and 22.6–25.5° for cycle 3); thus, for Ovda Regio, layover, foreshortening, and elongation are minimal, whereas radar shadow should be accentuated.

Geologic mapping and structural analysis. When performing geologic mapping, two distinct types of elements must be mapped: (a) lithologic units (rock types) and (b) morphological features. Lithologic units on Venus are limited to eolian deposits, impact crater ejecta, and volcanic flow units (e.g., Weitz 1992) and are identified in SAR images on the basis of radar brightness or emissivity, together with flow features such as lobes or flow fronts. Morphological features can be subdivided into primary structures (structures that accompanied deposition) and tectonic structures (structures that formed after unit emplacement and are not associated with emplacement). Primary structures can be used to characterize associated lithologic units and provide clues to unit emplacement. Primary structures include cinder cones, channels, lobate flow fronts, and impact craters. Tectonic structures reflect the kinematic evolution of a region and may place constraints on dynamic processes. Tectonic structures include wrinkle ridges, folds, fractures, and faults.

For lithologic units, we must be concerned with spatial distribution and depositional and temporal relations between distinct

units, or stratigraphy (e.g., Senske and Stofan 1993). Constructing a stratigraphic sequence of units requires knowledge of emplacement mechanisms. For example, lava flows, eolian units, and impact crater ejecta are successively deposited from above. Intrusive units can be emplaced across or between preexisting layers. In some cases, where clear embayment or superposition relationships between lithologic units are visible, it is possible to determine relative ages; in other cases, units abut against one another, and relative ages are impossible to determine. Primary structures can also help determine depositional sequence. Tectonic structures may be used in some cases to identify a depositional sequence; however, tectonic structures *may not* be used to identify lithologic units. For example, unit A, which exhibits wrinkle ridges, may be partially covered by unit B, which lacks wrinkle ridges. Unit A might be older than unit B, or the wrinkle ridges may not have formed in unit B, for some mechanical reason. The former is the simplest interpretation and the most likely, in the absence of evidence for the latter. Although wrinkle ridges or other tectonic structures may provide evidence for relative timing between units, they provide no absolute temporal constraints. Unit A may have existed for 1 day or for 1 Gy before wrinkle ridges formed.

Conversely, volcanic flow units might be useful for determining relative age relationships between structures. On Venus, flows are identified based on radar brightness and scattering characteristics, which result from roughness and slope as well as composition. Therefore, identification of a flow unit requires separation of the effects of slope from the effects of roughness and composition. This can be difficult in areas where structures, which are defined by slope, overlap spatially with flows. For example, a dark area between two fold crests may be dark because of its topographic relationship to the fold crests, or because it is filled by a smooth flow. In the absence of independent evidence it is not possible to distinguish between the two. In Ovda Regio, the presence of tectonic structures and the resulting high radar backscatter makes clear identification of flow units difficult. In general, areas that might be interpreted as flows show no consistent regional age relationships to each other or to tectonic structures and thus are not useful in determining the sequence of deformation at Ovda Regio at a regional scale (Hansen *et al.* 1998). In order for volcanic flow units to be useful in this capacity over an area the size of Ovda Regio, volcanism would have to have been continuous throughout the deformation process over the entire region, much as sedimentation is effectively continuous on Earth. Volcanic flow units in Ovda are localized and limited in areal extent and, as we outline in a later section, cover or embay most tectonic structures. In the absence of consistent and robust stratigraphic controls, then, unraveling Ovda's deformation sequence requires an understanding of the mechanisms responsible for forming tectonic structures.

A tectonic structural and kinematic analysis requires: (1) identification of structures using radar characteristics; (2) mapping the spatial distribution and orientation of structures; and (3) determination of temporal relations between structures. Step 3 generally cannot be accomplished solely by carrying out steps

1 and 2; one must also understand how each structure forms. For example, in the case of two intersecting lineaments, one of which terminates against the other, the relative order of formation of the two depends on what structures the lineaments represent. If they are dikes, the throughgoing lineament is younger, because dikes intrude across preexisting rocks (“cross-cutting relations”). However, if the lineaments are open fractures, the throughgoing lineament is older, because fractures cannot propagate across free surfaces. Thus to deduce structural temporal relations, it is necessary to understand deformation mechanisms. This type of analysis is the cornerstone of structural and kinematic work on terrestrial planets and icy satellites (e.g., McGill 1971, Golombek 1985, Banerdt and Golombek 1988, Golombek and Banerdt 1990, Tanaka *et al.* 1991, Banerdt and Sammis 1992). Once a mechanical basis for relative timing between structural elements is established, the resulting temporal history provides clues about deformation mechanisms. Such a temporal history is vital to understanding the implications of Ovda Regio’s structures for crustal plateau formation.

RESULTS OF THE STRUCTURAL AND KINEMATIC ANALYSIS

The Structures

Tectonic structures appear in SAR images as lineaments and surfaces. We determine the nature of these features based on their radar characteristics. Lineaments exhibit several types of characteristics. Single lineaments interpreted as fractures can appear as thin, straight, or anastomosing lines with uniform radar brightness and high tonal contrast with surrounding features (Ford *et al.* 1989, Stofan *et al.* 1993, Keep and Hansen 1994, Hansen and Willis 1996). Alternatively, single lineaments interpreted as fold crests can be wide, straight or curved, and radar bright along one side, with a gradual brightness transition across them (Solomon 1991, Stofan *et al.* 1993; Keep and Hansen 1994, Hansen and Willis 1996). This tonal gradation is most pronounced if the fold crest is oriented at a high angle to radar look direction. Areas between fold crests are commonly radar dark and may be locally filled by interpreted lava flow material, though this interpretation requires evidence above and beyond radar darkness (Keep and Hansen 1994, Hansen and Willis 1996, Hansen *et al.* 1998).

Lineaments may also be paired. In Ovda Regio, sets of paired lineaments define a system of alternating topographic troughs and ridges over much of the study area (Fig. 2). The lineaments defining trough walls show abrupt tonal transitions relative to the surrounding areas. This effect is accentuated for lineaments trending at high angles to radar look direction. Ridges and trough floors commonly have uniform radar brightness. Lava flows—so interpreted because of their uniformly radar-dark (hence smooth) surfaces and because they obscure structural lineaments—locally embay or flood troughs. Individual ridges and troughs are on the order of 1–3 km wide and up to

50–100 km long. The traces of trough-bounding lineaments on topography and other structures are approximately straight, suggesting steep trough walls. Trough walls generally end abruptly, forming parallel trough terminations in map pattern, though some join at their ends, forming V-shaped terminations in map pattern.

We interpret these ridge-and-trough morphological features to be correlative with the structures described by Hansen and Willis (1996, 1998), which they called “ribbons.” These workers described two structural end-member ribbon varieties: (a) tensile-fracture ribbons, which form by tensile fracturing and subsequent extension of a very thin brittle layer separated from a ductile substrate by a sharp décollement; and (b) shear-fracture ribbons, which form by normal faulting and subsequent extension of a similar thin brittle layer. Shear-fracture ribbons are essentially long, narrow, flat-floored graben. Diagnostic shear-fracture ribbon features are:

- (1) width of ridges and troughs, and thus, spacing (wavelength); Hansen and Willis (1998) reported shear-fracture ribbon wavelengths in Thetis Regio as 3.5–4.5 km (reflecting the distance from trough center to trough center), and we obtain similar values for Ovda Regio (Table 1);
- (2) aspect ratios; ribbon troughs commonly range up to 100 km in length, giving them extreme length-to-width aspect ratios;
- (3) approximate straightness of trough-bounding scarps, implying steep walls;
- (4) morphology of trough-bounding scarps; shear-fracture ribbons may display accommodation structures (multiple bright or dark lineaments) in their walls, and individual troughs are commonly difficult to trace due to the normal-fault character of their walls; tensile-fracture ribbons, by contrast, exhibit troughs bounded by single, well-defined scarps;
- (5) trough walls that cannot be exactly matched across individual troughs; tensile-fracture ribbons, by contrast, exhibit matching trough walls;
- (6) trough terminations; shear-fracture ribbon troughs terminate with trough floors ramping up to the level of ridges; tensile-fracture ribbons show V-shaped terminations;
- (7) penetrative, pervasive fabric defined by ribbons over thousands of square kilometers. Ovda’s ridge-and-trough structures show all of these characteristics; features 1–6 are shown in Figs. 2b and 2c and 3, and feature 6 is illustrated in Fig. 9. We conclude that Ovda’s ridge-and-trough structures are correlative with the shear-fracture ribbons of Hansen and Willis (1998).

Other sets of paired lineaments, found in spatial correlation with folds, commonly curve outward across fold crests and describe short (10–25 km), wide (5–10 km) lens-shaped depressions oriented perpendicular to fold axes (Fig. 3). Depression-bounding lineaments show uniform radar tonality and high contrast in radar brightness with surrounding terrain. Some floors exhibit uniform radar tonality, indicating that they are smooth and possibly flooded; others show multiple scarps defined by

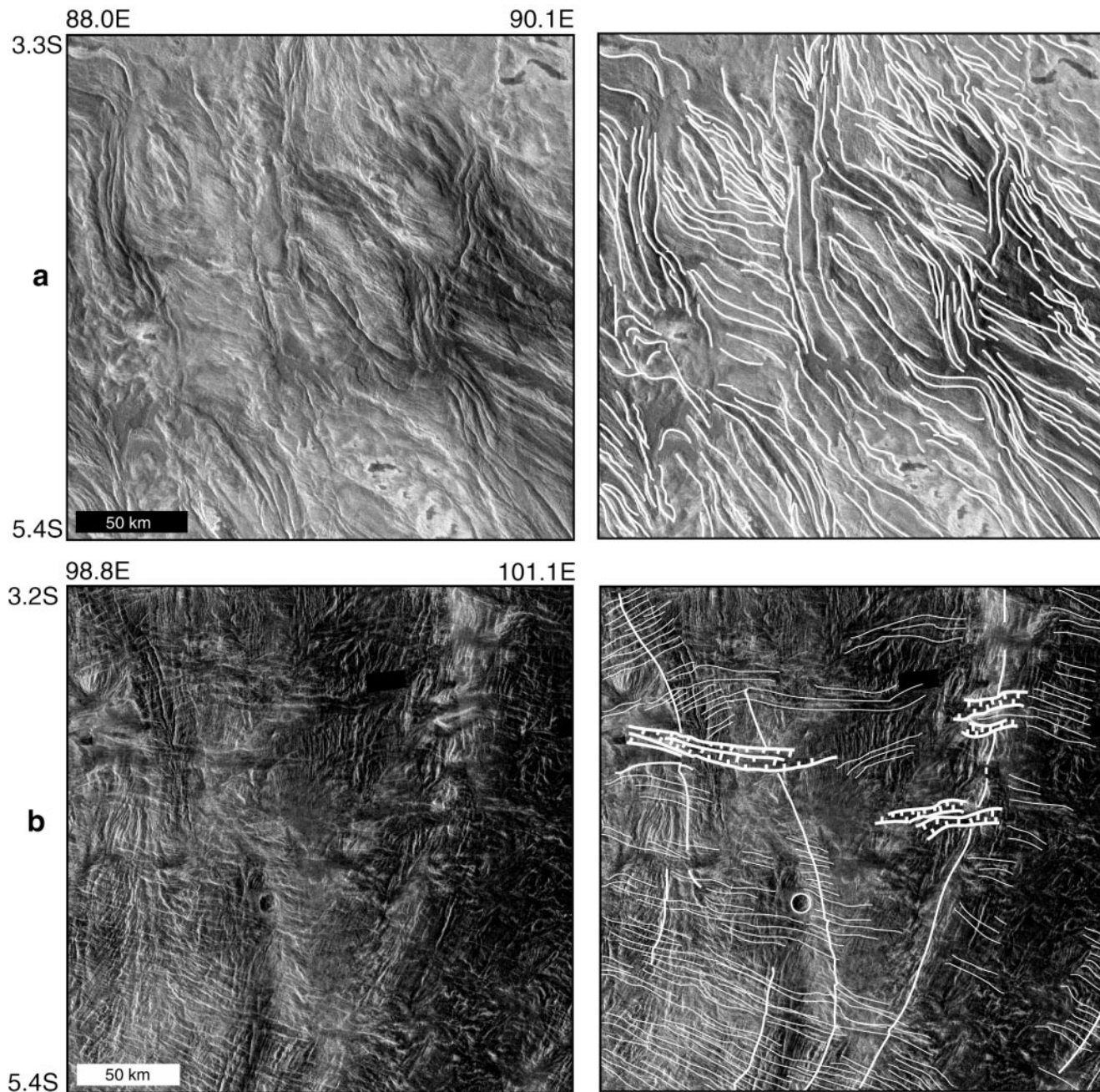


FIG. 2. Full-resolution SAR images (left) and structural maps (right) of examples of structural domains. Locations shown in Fig. 1. (a) Domain I (left-look image). Folds are the only structures present. Heavy lines show major fold trends; shorter-wavelength folds parallel larger folds but are too small to map. (b) Domain II (left-look image). Thin lines, ribbon troughs; heavy lines, folds; heavy ticked lines, graben; ticks denote lows. Circular feature in the center is an impact crater. (c) Detail of Domain II (right-look image). Heavy black solid lines, fold crests; thin ticked black lines, ribbon trough walls; heavy white ticked lines, graben; ticks denote lows. (d) Domain III (left-look image). Symbols same as (b).

radar-bright interior lineaments. We interpret these structures as graben (e.g., McGill 1971, Basilevsky *et al.* 1986, Solomon *et al.* 1991, Bindschadler *et al.* 1992a, Keep and Hansen 1994, Hansen and Willis 1996). Though ribbons and graben commonly occur in close spatial association, the two structures differ morphologically. Their differences are highlighted in Fig. 3; the detail in Fig. 3a shows several graben, illustrating their tendency to widen

at fold crests and their interior accommodation structures, and the detail in Fig. 3b shows shear-fracture ribbons, illustrating the characteristics listed above.

In order to describe the spatial distributions of ribbons, folds, and graben, we divide eastern Ovda into three structural domains (I, II, and III), distinguished on the basis of fold styles and orientations (Fig. 1). In the next sections we detail the

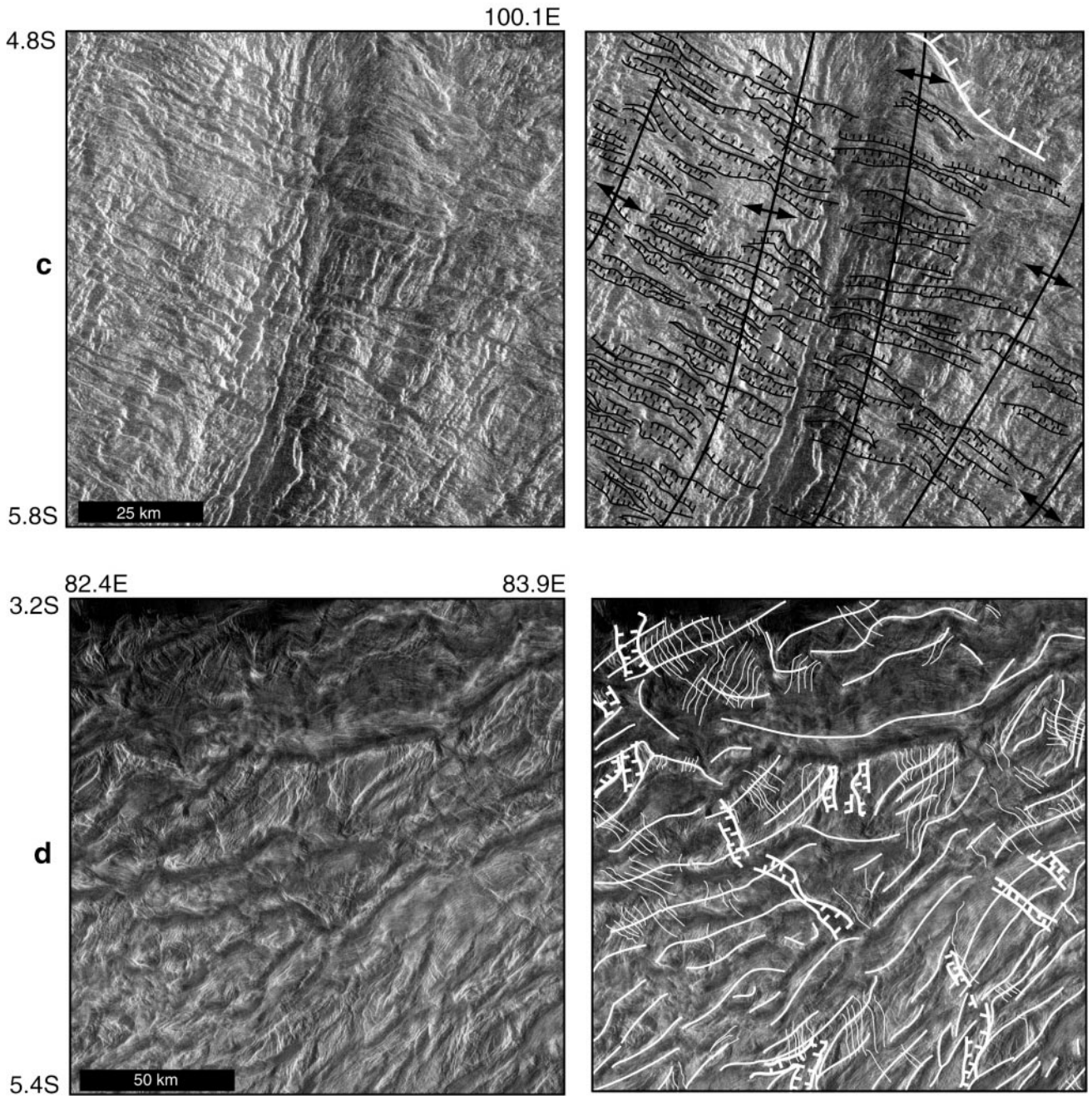


FIG. 2—Continued

characteristics, distribution, strain, and relative timing of structures in each domain.

Domain I

Domain I ($\sim 500 \times 400$ km, centered at $\sim 2.5^\circ\text{N}$, 87.5°E) hosts closely spaced, anastomosing folds (Figs. 1 and 2a). Fold wavelengths inferred from crest spacings range continuously from the limit of SAR resolution (~ 100 m) to 1 km. Fold crests mapped in Fig. 2a show major trends; many folds too closely

spaced to map at this scale parallel the larger folds. Fold lengths range up to 100 km and describe an overall chevron-shaped map pattern. This terrain has been called “lava flow terrain” because its structures resemble those of the surface of a terrestrial pahoehoe flow, though at a much larger scale (Hansen and Willis 1996). A data gap immediately west of Domain I obscures its western boundary.

In principle, it should be possible to determine heights of folds in Domain I using stereo methods (e.g., Plaut 1993a). However, this would require positive identification of identical

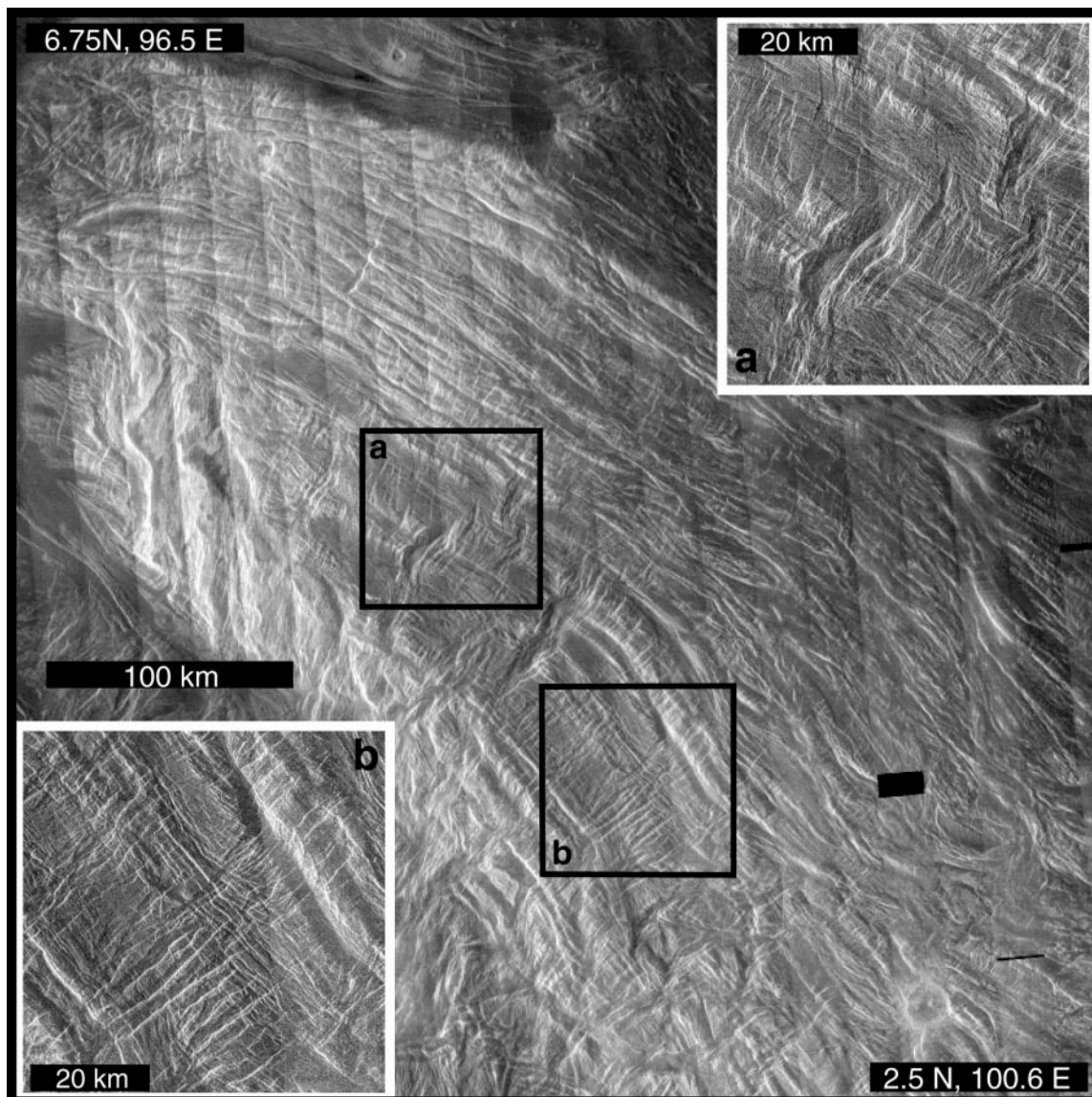


FIG. 3. (After Phillips and Hansen 1998): Full-resolution left-look SAR image of portion of NE fold margin of Ovda (Domain II) showing NW-trending folds, and NE-trending complex graben (a) and shear-fracture ribbons (b). Location shown in Fig. 1. Note morphological differences between ribbons and graben; see text for details.

points on fold crests and troughs in a stereo pair of images. Domain I folds are too tightly spaced and too small to be accurately resolved in this way; furthermore, it is nearly impossible to unequivocally identify identical points on fold crests or troughs in two images. Neither can the parallax method of Connors (1995) be applied, because this method is derived for discretely dipping surfaces, and there is no evidence that Domain I fold limbs are straight. Layover effects at the equator are minimal due to high radar incidence angles; furthermore, use of layover to quantify fold heights requires an unambiguous base level at a known elevation relative to the fold crest, such as a lava flow that has flooded all around a fold. This situation

does not exist in Domain I. The extremely close fold spacing in Domain I, however, suggests that fold heights are at most equal to their wavelengths, or 100 m to 1 km. Without robust constraints on fold amplitude, we cannot calculate interlimb angles or estimate the shortening accommodated by these folds. However, using empirical fold wavelength to layer thickness ratios of 3–6 (Sherwin and Chapple 1968, Smith 1977, Huddleston and Lan 1995, Kobberger and Zulauf 1995), we can estimate that Domain I folds reflect shortening of a layer 20 to 300 m thick. Furthermore, the fold axes' multiple orientations indicate constriction, or shortening along two of the three principal strain axes.

Domain II

Domain II occupies the northern, northeastern, and eastern topographic plateau boundaries and hosts ribbons, folds, and graben (Figs. 1, 2b, and 3).

Folds. Folds are long (up to 300–400 km) with arcuate traces and wavelengths (inferred from crest spacing) of 15–30 km (Figs. 2b and 2c). Folds with wavelengths ~ 5 km parallel large folds, occurring along and between large fold crests. Polyharmonic folds of this type can result from folding a package of rock with internal layers of different thicknesses, such as a layered flow unit; the smallest wavelength folds are parasitic folds (Ramsay and Huber 1987). As in Domain I, it is not practical to determine absolute fold amplitudes using layover or parallax differences; however, we can estimate a likely range. Both fold crests and troughs are exposed at the surface, indicating that the total relief resulting from the folds is less than or equal to the plateau relief at the location of the folds. Topographic profiles through Ovda's northeastern fold margin show total relief of ~ 0.5 km (Bindschadler *et al.* 1992a); thus fold amplitudes at that location (half the vertical distance from crest to trough) are likely less than or equal to 0.25 km. Due to the ~ 10 -km footprint of Magellan altimetry data for Ovda Regio (Plaut 1993b), we allow for the possibility that the total relief in Domain II is as great as 1 km, corresponding to a fold amplitude of 0.5 km. Thus we take 0.5 km as the maximum probable value for Domain II fold amplitudes. If we approximate fold limbs as planar, and assume that the folded layer has uniform thickness, the interlimb angle is given by

$$i = 2\text{atan}(\lambda/2A), \quad (1)$$

where i is interlimb angle, λ is fold wavelength, and A is fold amplitude. If $A = 0.5$ km and $\lambda = 10$ –30 km, interlimb angles are 169° to 176° , and limb dips are 6° to 2° . Folds of this character are classified as “gentle” (Ramsay and Huber 1987, Twiss and Moores 1992).

We estimate shortening as follows. Elongation of a line length in a particular direction is defined as

$$e = (l_f - l_i)/l_i, \quad (2)$$

where l_f and l_i are final and initial line lengths, respectively, and e is fractional elongation (negative values indicate shortening). In order to apply this equation to Domain II folds, we assume: (1) that the shortened layer maintained a constant thickness during shortening (parallel-style folding) and (2) that there was no homogeneous layer shortening prior to folding. These assumptions imply that shortening is entirely accommodated by folding and therefore provide minimum strain estimates. In terms of fold amplitude and wavelength, Eq. (2) becomes

$$e = \frac{\lambda/2 - \sqrt{A^2 + (\lambda/2)^2}}{\sqrt{A^2 + (\lambda/2)^2}}. \quad (3)$$

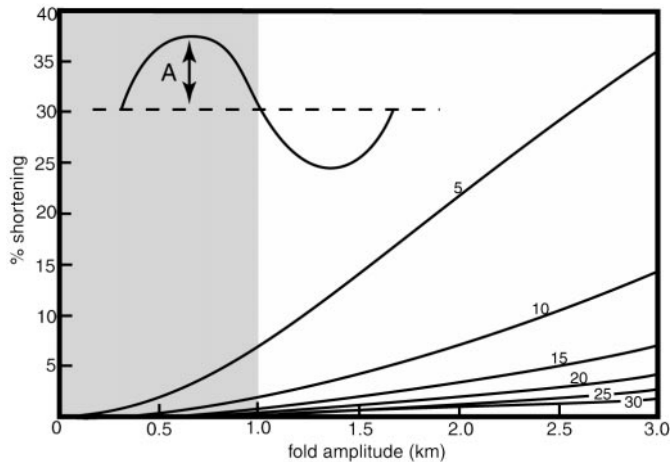


FIG. 4. Plot of shortening versus fold amplitude in Domains II and III. Curves correspond to fold wavelengths in km. Gray area represents the most likely fold amplitudes. Note that amplitude is defined as half the vertical distance from fold trough to crest.

The most likely maximum estimates of shortening (using $A = 0.5$ km) for Domain II folds range from 0.1% for 30 km wavelength folds to 0.5% for 10-km wavelength folds (Fig. 4). Even if $A = 1$ km (which is unlikely), shortening estimates increase only to 0.2% for 30 km wavelength folds and 2% for 10 km wavelength folds.

The regular spacing of Domain II folds reflects competent layer thickness (e.g., Sherwin and Chapple 1968, Smith 1977, Solomon and Head 1984, Huddleston and Lan 1995, Kobberger and Zulauf 1995). Folds with 15- to 30-km wavelengths yield competent layer thickness estimates of 2.5–10 km using empirical wavelength-to-layer thickness ratios of 3–6. We interpret the base of the regional competent layer to be at or above the brittle–ductile transition (BDT); that is, the depth to the BDT in this region is greater than or equal to the competent layer thickness. Brown and Grimm (1997) estimated the depth to the BDT for folds in Ovda with 15 km wavelength at ~ 5 km using thermal gradient considerations; the same calculation performed using larger wavelengths would yield a deeper BDT. The Brown and Grimm (1997) value falls within our estimated range.

Ribbons. Shear-fracture ribbons occur throughout Domain II (Figs. 2b, 2c, and 3). They typically trend perpendicular to fold crests. Locally, two nearly orthogonal ribbon sets are present; the dominant set trends subnormal to fold crests. Ribbon troughs and ridges track across folds of all wavelengths with no obvious change in width, spacing, or trend correlating with fold crests or valleys. Trough walls are roughly parallel across folds; ribbon troughs, unlike large graben, generally do not widen significantly across fold crests (Fig. 3; Hansen and Willis 1996, Phillips and Hansen 1998, Fig. 1). Ribbon wavelengths are uniform over the domain.

As outlined in Hansen and Willis (1998), Ovda's shear-fracture ribbons are in fact long, narrow, graben (Fig. 5a). Because

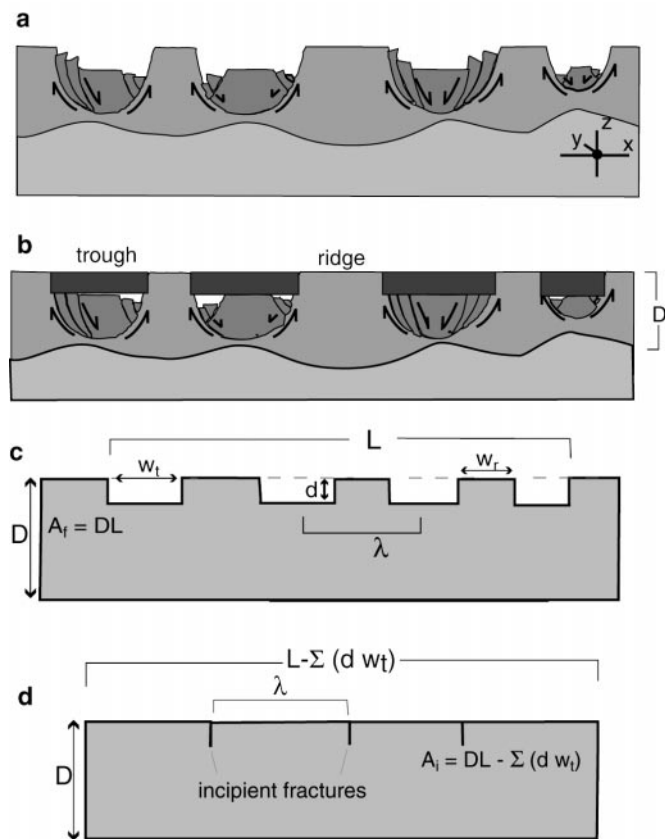


FIG. 5. Schematic cross-section of shear-fracture ribbons showing orientations of principal strain axes ($x > y > z$). (b) Schematic diagram illustrating trough and ridge definitions, and competent layer thickness. (c) Block diagram showing parameters used in calculating layer thickness and extension: L , transect length; D , layer thickness; w_t and w_r , trough and ridge widths, respectively; d , trough depth; λ , structural wavelength; and A_f , final block area. (d) Block diagram of ribbon terrain prior to extension. A_i , initial block area.

ribbons comprise a class of feature morphologically distinct from Ovda's complex lens-shaped graben, we distinguish between ribbons and graben to avoid the a priori assumption that the two features have the same genetic origins. We retain the term "ribbons" instead of "graben" to avoid confusion in referring to these features.

In many locations, as in Figs. 2b and 2c, ribbon troughs trend subparallel to the radar look direction. This orientation, together with the narrowness of trough-bounding lineaments and the fact that layover effects are minimal in Ovda make it impossible to conduct a radargrammetric analysis similar to that of Hansen and Willis (1998) to determine ribbon wall heights or dips. The morphological and scale similarities between ribbons in Ovda and Fortuna suggest that Hansen and Willis' values of 250 m for wall heights and 75–90° for wall dips may be appropriate estimates for Ovda's ribbons, though shallower dips may be possible. The fact that trough-bounding lineaments do not systematically deviate over fold crests suggests that trough walls are steep. Bindschadler *et al.* (1992a,b) described structures in

Alpha and Ovda regions that fit the description of shear-fracture ribbons outlined above, calling them "steep troughs" in Ovda and "parallel grabens and grooves" in Alpha. These workers inferred trough-bounding scarp heights of "no more than several hundred meters" for ribbons in Alpha, and interpreted Ovda's trough-bounding scarps as steeply dipping, consistent with our interpretations.

Ribbon fabric characterizes all of Domain II. In order to understand the significance of this fabric, we must determine how much extension is accommodated by ribbons and how it is partitioned. Because ribbons are regularly spaced (Figs. 2, 3), their structural wavelength reflects competent layer thickness at the time of their formation. Hansen and Willis (1998) used wavelength instability analysis to deduce competent layer thickness during ribbon formation with terrestrial boudins as a mechanical analog. Boudins form in a competent layer embedded in or overlying a less competent matrix, subjected to layer-normal flattening (e.g., Ramberg 1955, Rast 1956, Ghosh 1988, see Price and Cosgrove 1990 for a review). Boudins show both tensile-fracture and shear-fracture characteristics. Field observations and analog experiments indicate that boudin wavelength-to-layer thickness ratios are generally 2–4 for brittle boudins, and as high as 10–20 for pinch-and-swell structures in which ductile flow dominates (e.g., Talbot 1970, Price and Cosgrove 1990, Kobberger and Zulauf 1995, Kidan and Cosgrove 1996). These two end-member ratios, when applied to ribbons, provide bounds on layer thickness during Domain II ribbon formation. To use these ratios accurately, however, we must know the wavelength(s) of incipient shear failure prior to layer fracturing. However, only the final state is preserved at Ovda Regio; and because shear-fracture ribbons are not tensile fractures, we cannot simply match trough walls to reconstruct the initial state (Hansen and Willis 1998). To address this issue, we infer ribbon wavelengths using the distance from trough center to trough center. This wavelength exceeds the incipient fracture wavelength because it includes some unknown amount of finite extension (Figs. 5b and 5c). Therefore our wavelength measurements are *maximum* values, resulting in *maximum* layer thickness estimates and *minimum* extension estimates, regardless of the wavelength-to-layer thickness ratio used. Although ribbons define a coherent pattern over the entire domain, folds, fine-scale lineaments, areas of high radar backscatter, and lava flows locally obscure ribbon details. Furthermore, ribbons commonly trend parallel to the radar look direction. All of these factors influence our ability to measure long uninterrupted transects. For analysis, therefore, we chose transects which exhibit continuous "exposure" of ridges and troughs. We measured ribbon trough and ridge widths directly from digital FMIDR SAR images for four transects through Domain II (Table I). We define a trough as the area between the outermost edges of a pair of trough-bounding lineaments (Fig. 5b). We choose this definition because it allows us to unambiguously determine trough boundaries in SAR images, whereas attempting to locate the center of a trough by eye would lead to error. Thus our transects begin and

TABLE I
Data and Mean Wavelengths for Six Transects through Ribbon Terrain in Domains II and III

Transect	Start/end lat/lon	$N_r = N_t$	w_{rm} (km) \pm st dev	w_{tm} (km) \pm st dev	λ_m (km) \pm st dev
Iia	3.75N, 98.67E	12	1.14 ± 0.55	2.38 ± 0.84	3.55 ± 0.95
Left look	3.40N, 39.98E				
Iib	5.20S, 99.52E	12	1.40 ± 0.84	2.80 ± 0.80	4.19 ± 1.1
Right look	5.67S, 99.40E				
Iic	5.10S, 99.65E	18	1.14 ± 0.72	2.63 ± 1.2	3.80 ± 1.0
Left look	5.70S, 99.35E				
Iid	8.85S, 79.75E	33	1.81 ± 1.2	1.54 ± 0.89	3.35 ± 1.5
Left look	8.85S, 80.80E				
IIIa	6.15S, 93.52E	15	1.62 ± 0.90	2.13 ± 1.6	3.80 ± 1.5
Right look	6.62S, 93.00E				
IIIb	2.90S, 82.95E	16	1.62 ± 0.90	1.87 ± 1.0	3.38 ± 1.3
Left look	3.15S, 82.45E				

end at the outer edges of troughs. Wherever ribbon trough and ridge widths can be measured, their ratios are consistent with those obtained for the chosen transects, giving similar wavelengths; therefore estimates of layer thickness and extension obtained using transect data apply to ribbons outside transect limits (e.g., Table II). Mean wavelengths for four individual transects range from 3.4 to 4.2 km, with an overall mean of 3.7 km (Table I). This mean value yields maximum layer thickness estimates of 0.9–1.9 km, using the brittle wavelength-to-layer thickness ratios of 2–4, and estimates of 0.2–0.4 km using the ductile ratios of 10–20. These values are end-member estimates; in either case, ribbon wavelengths suggest that ribbons deformed an extremely thin competent layer. This conclusion is also consistent with previous analysis; Bindschadler *et al.* (1992b) concluded that the “narrow width and spacing” of shear-fracture ribbons in Alpha suggests a mechanical decollement at depths of 1–5 km, though they do not provide details concerning their estimate of depth to the mechanical discontinuity.

The mechanical discontinuity at the base of the brittle, ribbon-forming layer could represent one of two things: (a) a weak layer within the crust, underlain by another strong layer or (b) the BDT. If (a) were the case, we would expect to see a second wavelength of extensional structure, also regularly spaced, superimposed on

the existing ribbon fabric. We do not observe such a fabric. It is also possible that the weak layer during ribbon formation was so thick that it absorbed all the strain experienced by the strong layer extending at depth; but this is in effect the same as option (b). Thus we treat the base of the competent layer during ribbon formation as equivalent to the BDT.

Gilmore *et al.* (1998) also mapped shear-fracture ribbons at various locations in Ovda Regio. These authors’ mapping and interpretation agree with ours on several points: (1) The features Gilmore *et al.* (1998) mapped are the same features as our shear-fracture ribbons; these authors used the same criteria for identifying these structures as those outlined above in Hansen and Willis (1998). Furthermore, they report trough widths of 1–3 km, in agreement with our trough width estimates. (2) The features are extensional. These authors call shear-fracture ribbons “graben”; for the reasons outlined above, we retain the term “ribbons.” (3) The features are regularly spaced. The mapping of Gilmore *et al.* (1998) reflects a structural wavelength in agreement with our estimates (their Figs. 7, 8). (4) The features terminate at a mechanical discontinuity.

The analysis of Gilmore *et al.* (1998) also disagrees with ours on two major points: (1) Gilmore *et al.* (1998) do not distinguish between ribbons and larger complex graben, in spite of morphological dissimilarities (our Figs. 2b, 2d, and 3; Bindschadler and Head 1991, Bindschadler *et al.* 1992a, Solomon *et al.* 1992, Hansen and Willis 1996, 1998, Phillips and Hansen 1998, Hansen *et al.* 1998). Identifying ribbons and graben as equivalent structures leads Gilmore *et al.* (1998) to conclude that ribbons and graben formed synchronously and by the same mechanism. (2) Gilmore *et al.* (1998) do not address the structural wavelength of ribbon fabric. Instead, following on (1), they assume a triangular geometry for an individual ribbon/graben, using a range of bounding fault dips of 60–75° and widths of 0.5–5 km, and calculate the depth to the meeting point of the bounding faults trigonometrically (their Fig. 1a). The authors argue that this meeting point is located at a mechanical discontinuity. The

TABLE II
Data for Five Transects in Domain II
Parallel to Transect Iia

Iia subtransect	λ_m (km)
a	3.55
b	3.61
c	4.01
d	3.11
e	3.17
Mean	3.49
st dev	0.37

resulting layer thickness estimates encompass a range from 0.5 to 9 km. We disagree with this approach. First, regardless of bounding fault dips or widths of individual structures, shear-fracture ribbons in this region define a coherent, penetrative fabric, and it is therefore the structural wavelength which reflects layer thickness and not the geometry of an individual structure. Second, the larger, complex graben are not regularly spaced and so do not define a coherent fabric and thus have no discernible structural wavelength. These structures should be distinguished from the ribbons on this basis, in addition to their morphological differences (Hansen and Willis 1998, Phillips and Hansen 1998, Hansen *et al.* 1998). Therefore, the Gilmore *et al.* (1998) reported range of 0.5–9 km for layer thickness, derived assuming that ribbons and graben are the same structure, is not valid. Thus we maintain that shear-fracture ribbons are distinct from complex graben, and reflect a shallow BDT at the time of their formation.

Ribbon extension can be estimated using Eq. (2). Assuming plane strain (that is, no extension along ribbon trend), shear-fracture ribbon extension occurs by motion of trough material in two dimensions: parallel to the trend of the transect (x) and vertically (z) (Fig. 5a). In an x - z cross section, elongation (e) becomes

$$e = (A_f - A_i)/A_i, \quad (3)$$

where A_f and A_i are the final and initial x - z cross-sectional areas, respectively. The final area, A_f , is

$$A_f = DL,$$

(Fig. 5c) where D is layer thickness and L is transect length. The initial area, A_i , is

$$A_i = DL - d \sum w_t,$$

(Fig. 5d) where d is trough depth and w_t is trough width. Assuming uniform trough depths along a transect, elongation is

$$e = \frac{d \sum w_t}{DL - d \sum w_t}.$$

L can be expressed as the sum of ridge widths and trough widths, yielding

$$e = \frac{d \sum w_t}{D \sum w_t - d \sum w_t + D \sum w_r}.$$

Expressing elongation in terms of d/D and $\sum w_r/\sum w_t$,

$$e = \frac{d/D}{1 - d/D + \sum w_r/\sum w_t}.$$

Finally, $\sum w_r/\sum w_t$ can be expressed as $N_r w_{rm}/N_t w_{tm}$, where N_r and N_t are number of ridges and number of troughs, respectively, and w_{rm} and w_{tm} are mean ridge and trough widths, respectively:

$$e = \frac{d/D}{1 - d/D + (N_r w_{rm}/N_t w_{tm})}.$$

For our transects, $N_r/N_t = 1$. Thus,

$$e = \frac{d/D}{1 - d/D + w_{rm}/w_{tm}}. \quad (4)$$

Therefore extension depends on the ratios d/D and w_{rm}/w_{tm} . We can directly determine the ratio w_{rm}/w_{tm} , and we have estimated maximum values for D to be 0.9–1.9 km. We evaluate Eq. (4) for various values of trough depth to competent layer thickness ratio, d/D (Fig. 6). Extension estimated in this manner ranges from ~5 to 65% over the domain. Extension estimates are not well-constrained because (a) our structural wavelength estimates do not include finite extension of ribbon troughs, as outlined above, and (b) extension depends on trough depths, which are not well known. However, regardless of the absolute amount of extension, ribbon fabric represents penetrative extension, distributed over the entire domain. This is the critical constraint on deformation mechanisms.

Graben. Graben in Domain II cut fold crests and are oriented with their long axes perpendicular to fold crests (Figs. 2b, 2d, and 3). Graben range from ~25 to 75 km long and are ~5–15 km wide at the center, with length-to-width aspect ratios of 5–15. Graben commonly widen substantially over fold crests and accommodate limited, localized extension. Graben spacing is not periodic; therefore we cannot deduce competent layer thickness at the time of graben formation using graben wavelengths.

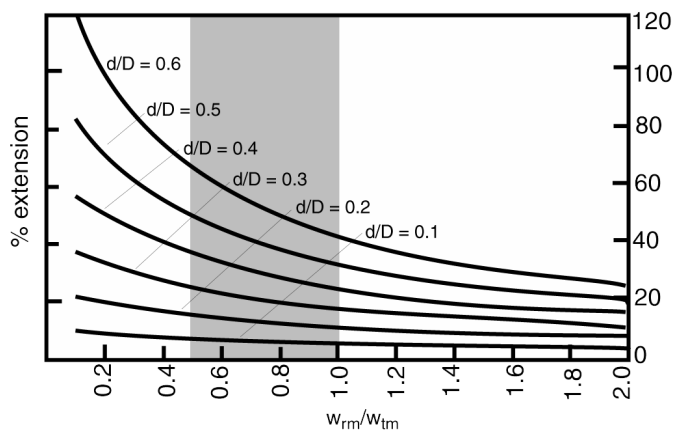


FIG. 6. (a) Plots of extension versus mean ridge width: mean trough width ratios (w_{rm}/w_{tm}) for various values of trough depth: competent layer thickness ratios (d/D). Range of w_{rm}/w_{tm} appropriate for Ovda Regio shown in gray.

Temporal relations. Ribbons, folds, and graben overlap spatially in Domain II. Lava flows do not interact with ribbons, folds, and graben regionally such that it is possible to use cross-cutting or superposition relations to determine consistent temporal relations across Ovda. Distinct flows outside lava-flooded basins, when identifiable, are limited and localized. The majority of lava flows within and outside basins are cut only by complex graben (Banks and Hansen 1998). Several of Ovda's interior lava-flooded basins show complex magmatic and deformation histories, possibly indicating several phases of both processes, and some indicate reactivation of previously formed structures. A detailed analysis of these basins and flows is outside the scope of this work. However, flooded intratessera basins developed dominantly late relative to ribbon, fold, and complex graben formation (Banks and Hansen 1998).

Ribbons and folds are spatially correlative in Ovda Regio. In the absence of robust stratigraphic constraints, (e.g., those provided by continuous sedimentation or volcanism), it is not possible to determine which structure formed first without understanding the mechanical conditions necessary for each structure to form (as outlined under Methodology). Thus we examine mechanical requirements for formation of ribbons, folds, and graben.

Graben generally reside at fold crests, are oriented with their long axes perpendicular to fold axes, and widen over fold crests, indicating that graben postdate folds in Ovda Regio (e.g., Bindschadler *et al.* 1992a, Hansen and Willis 1996; see also McGill 1971 for similar analysis of lunar graben).

Hansen and Willis (1998) examined in detail each of the possible temporal relations between ribbons and folds. They considered three possibilities: (1) ribbons predate folds; (2) ribbons form coevally with folds; and (3) ribbons postdate folds. They concluded on the basis of ribbon–fold geometry and the differences in depth to BDT reflected by ribbons versus folds that ribbons most likely predate folds in their study areas. We have demonstrated here that the ribbons and folds at Ovda Regio display the diagnostic characteristics of crustal plateau ribbons and folds outlined by Hansen and Willis (1998), and we can therefore apply the ribbon–fold temporal relations derived in that work to Ovda. We summarize those results as they pertain to Ovda Regio below.

If Ovda's shear-fracture ribbons have walls that dip 60°, we would expect ribbon troughs to widen at fold crests if ribbons postdate folds. Ovda's ribbon troughs do not systematically widen at fold crests (Figs. 2, 3); thus they (a) predate folding, (b) have steeply dipping walls, or (c) both.

Ribbon wavelengths indicate that ribbon formation required a very thin competent layer (≤ 0.9 – 1.9 km) over a ductile substrate. The BDT during folding (at least 2.5–10 km) was deeper than during ribbon formation, resulting in greater strength to deeper levels. A return of the BDT to ribbon-forming depth after folding would likely cause relaxation of long-wavelength folds, as illustrated by rheological profiles of the crust (Fig. 7). Even if this difficulty could be avoided (e.g., by a sudden change

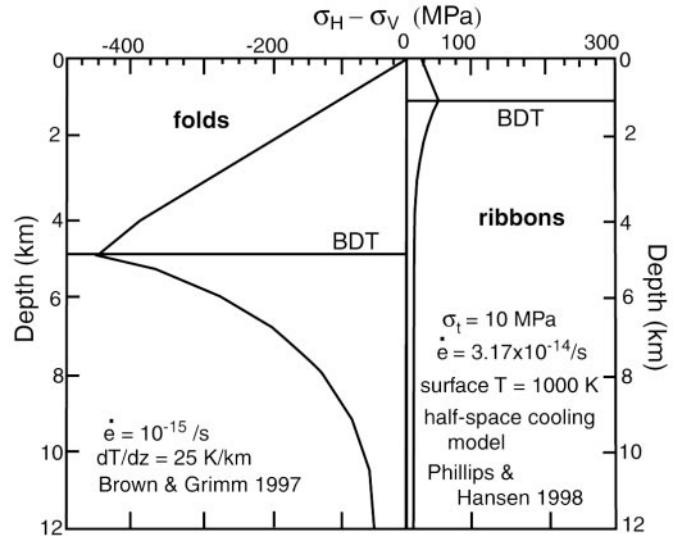


FIG. 7. Rheological profiles through venusian crust for ribbon formation (right; Phillips and Hansen 1998) and for folding (left; Brown and Grimm 1997). Tension is positive, compression is negative; BDT, brittle–ductile transition.

in strain rate), the formation of ribbons after folds would require formation of a folded décollement, at a uniformly shallow depth over the entire (several thousand km²) domain. Above the folded décollement, the crust would extend, forming ribbons, with extension below the décollement occurring in a different manner. Gravitational relaxation might result in extension following contraction; however, extensional structures would (a) likely be oriented parallel to fold axes, or (b) if oriented at high angles to fold axes, would be lens-shaped graben cutting fold crests. Ovda's ribbons are oriented at high angles to fold axes, but are not lens-shaped and extend across multiple fold crests and valleys, apparently unaffected by local fold topography (see additional discussion under Overall Patterns). We conclude, as did Hansen and Willis (1998), that the most plausible hypothesis is that ribbons predate folds.

It is possible for a single competent layer in constriction to simultaneously form mutually perpendicular folds and boudins. Kobberger and Zulauf (1995) experimentally produced perpendicular buckle folds and boudins in a Plasticene layer embedded in an incompetent matrix subjected to compression in two dimensions. The resulting boudin wavelengths were comparable to or larger than the resulting fold wavelengths. In Ovda Regio, ribbon wavelengths are typically an order of magnitude smaller than fold wavelengths, indicating different layer thicknesses for ribbon versus fold formation. Folds and ribbons could have formed synchronously with the observed wavelengths if two distinct competent layers were deformed, one at the surface and one at depth. This situation would likely result in two or more distinct wavelengths of both contractional and extensional structures, which is not observed.

Thus, the data are consistent with the interpretation that ribbons formed diachronously with folds and graben and that each

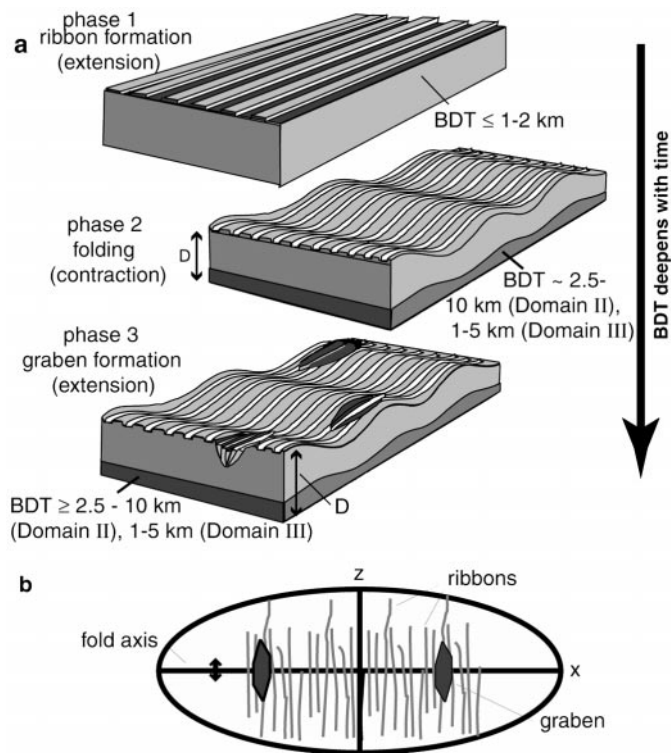


FIG. 8. (a) Block diagrams illustrating the three phases of Domain I deformation: ribbon formation (extension), folding (contraction), and graben formation (local extension). (b) Strain ellipse showing relative orientations of ribbons, folds, and graben at any point in the marginal fold domain. x and z represent maximum and minimum principal strains, respectively.

phase of deformation was characterized by a competent layer with a unique thickness range. The most likely timing of structure in Domain II is (1) ribbons, (2) folds, and (3) graben, each step representing an increase in depth to BDT. Our data provide no absolute constraints on the duration of ribbon formation relative to the duration of folding or on the length of time elapsed between phases.

Strain history. Domain II records a three-phase strain history (Fig. 8; Table III): (1) flattening normal to a thin brittle layer ($\leq 0.9-1.9$ km) which fractured and extended to produce ribbons; (2) minor contraction ($<5\%$) of a thicker competent layer ($2.5-10$ km), expressed as concentric folds; and (3) minor extension localized at fold crests, resulting in graben. A single bulk strain ellipse can account for ribbons, folds, and graben at any location, implying that all three phases could record progressive deformation with similar regional orientations of principal stress axes (Fig. 8b). Therefore it is not necessary to call on multiple deformation events to explain Domain II structures.

During Domain II deformation, the BDT migrated downward through the crust with time. Furthermore, progressive thickening of the competent layer involved in the deformation suggests that the BDT also widened as it deepened—that is, the zone

accommodating the transition from brittle to ductile behavior likely widened with time as it deepened. The evolution of the BDT as reflected by surface structures must be addressed by models of Ovda's formation and evolution.

Domain III

Domain III, located both west of Domain I and between Domains I and II (Figs. 1 and 2d), also hosts ribbons, folds, and graben.

Folds. Domain III folds differ from Domain II folds in terms of orientation and length; fold trends vary, giving the region a "basin and dome" appearance (Ramsay and Huber 1983, Chap. 4; Hansen and Willis 1996). Folds are generally short ($\sim 25-50$ km) with 5- to 15-km wavelengths (Fig. 2d). The same radar characteristics define folds in this domain as in the others. In the eastern region of Domain III, folds trend dominantly NE and NW; in the western region, folds trend dominantly NE, with some trending N to NW. This apparently disorganized map pattern is characteristic of interference folding, which can result either from constriction or multiple episodes of deformation of a competent layer (Ramsay and Huber 1983, 1987). The pattern preserved in Domain III is consistent with a single episode of constrictional layer-parallel deformation (see Ramsay and Huber 1983, p. 66, Fig. 4.11E). Following the same reasoning as for Domain II, a maximum value of $A = 0.5$ km and $\lambda = 5-15$ km yield interlimb angles of $157-172^\circ$, limb dips of $11-4^\circ$, and shortening of $2-0.2\%$ (Fig. 4). For each orientation of folds, spacing is regular, and we apply the same wavelength calculations as for Domain II folds. Fold wavelengths of $5-15$ km and wavelength to layer thickness ratios of $3-6$ yield competent layer thickness estimates of $\sim 1-5$ km.

Ribbons. Domain III ribbons differ from Domain II ribbons only in that they are more difficult to trace due to the disorganized nature of spatially overlapping folds, leading to higher radar backscatter. Ribbons track undeviating over folds of various wavelengths and orientations. We measured two ribbon transects through Domain III to determine competent layer thickness and extension (Table 1, Fig. 6). The overall mean wavelength for these transects is 3.6 km, corresponding to maximum layer

TABLE III
Compilation of Structural Data for Domains I, II, and III

Domain	Structures	Strain type	Elongation	Depth to BDT (km)
I	Interference folds	Contraction	?	0.02–0.3
II	Ribbons	Extension	5–65%	$\leq 0.9-1.9$
	Concentric folds	Contraction	$< -5\%$	2.5–10
	Graben	Extension	?	$\geq 2.5-10$
III	Ribbons	Extension	5–50%	$\leq 0.9-1.8$
	Interference folds	Contraction	$\leq -5\%$	$\sim 1-5$
	Graben	Extension	?	$\geq 1-5$

thickness estimates of 0.9–1.8 km, and minimum layer thickness estimates of 0.2–0.4 km. The ratios $w_{\text{tm}}/w_{\text{tm}}$ for the two transects are 0.76 and 0.87, yielding extension estimates of 5–50%, again depending on trough depth. These extension estimates are similar to those obtained for Domain II. Ribbon characteristics are uniform throughout the domain; wherever ribbon troughs and ridges are visible, their width ratios are consistent with the mean transect values. Thus, layer thickness and extension estimates calculated using transect data apply to the entire domain.

Graben. Domain III graben are similar to Domain II graben but are locally more sinuous (Fig. 2d). Domain III graben trend normal to fold axes and cut fold crests.

Temporal relations. By the same arguments presented for Domain II, the most likely deformation sequence in Domain III is ribbons, and then folds, and then graben. Graben occur perpendicular to fold axes, cut fold crests, and widen at fold crests, indicating that graben postdate the folds. Ribbons (1) show no tendency to widen at fold crests, (2) have structural wavelengths that indicate formation within a thin (≤ 0.9 –1.8 km) competent layer, and (3) show no evidence that their morphology or character was affected by local fold topography or orientation (Fig. 9). Folds deformed a generally thicker (1–5 km) competent layer. The difference between competent layer thickness for ribbons and folds in Domain III is not as pronounced as in Domain II, but folding prior to ribbon formation would still require migration of the BDT toward the surface following fold formation and would likely lead to patterns of ribbon extension controlled by local fold topography and orientation. Thus, the simplest and most direct interpretation of the data is that ribbons predated folds in Domain III.

Strain history. Domain III records (1) flattening normal to a thin layer, which fractured and extended to produce ribbons; (2) layer-parallel constriction of a thicker competent layer, resulting in interference folds; and (3) limited extension localized at fold crests, resulting in graben (Fig. 8; Table III). Structural wavelength-to-layer thickness ratios allow estimation of layer thicknesses for each of these three phases. These estimates, together with the temporal relations among structures, indicate that competent layer thickness, and thus the depth of BDT, increased as the deformation progressed.

Overall Patterns

Just as structural domains provide a useful way of interpreting local patterns and strain histories, overall structural patterns across and between domains provide fundamental constraints for Ovda's evolution as a whole.

Structural patterns. Ribbons, absent only in Domain I, define a broadly radial pattern relative to the plateau boundaries over most of the study area (Figs. 9a and 9c). They define a coherent spatial pattern over the study area, crossing the boundaries between Domains II and III with no change in trend, width, spacing, or geometry, unaffected by the changing character of folds at the boundary. The margins of Domain I are largely obscured by

a data gap to the west and by lava flows to the northeast. Where the Domain I–Domain II boundary is visible, ribbons fade out toward the boundary.

Folds vary in wavelength and trend between domains (Figs. 9b and 9c); fold orientation and style distinguish domains from one another. Closely spaced anastomosing folds characterize Domain I, whereas Domain II hosts long-wavelength folds, which form a concentric map pattern coincident with the topographic plateau margins. Mid-wavelength folds of several orientations characterize Domain III.

Graben are limited to large fold crests in Domains II and III, with their long axes perpendicular to fold axes. Graben do not form a discernible pattern independent of folds and so do not define or distinguish between structural domains.

Domain II folds, which define the boundaries of the deformation, are limited to plateau topography and do not extend into the plains; ribbons and graben are also confined to the plateau. Furthermore, Domain II folds are coincident with and parallel to the plateau's topographic boundaries. The "contact" (not a lithologic contact) between deformed high topography and surrounding volcanic plains does not show clear volcanic embayment relationships; there are no clear visible large-scale embayment relationships between the marginal fold belts and surrounding volcanic flows. Local lava flooding within the marginal fold belts is largely restricted to contained basins bounded by folds and/or fault scarps. Because Ovda's intratessera basins are not physically connected to exterior plains, there is no evidence to suggest that basin fill represents invasion of plains lava from outside the plateau's boundaries (Fig. 1). Ovda is thus a structurally bounded plateau.

Temporal relations. As we have outlined above, ribbons most likely predate all other tectonic structures in each of the domains. Furthermore, ribbons form a coherent structural pattern over the entire area; ribbons in Domain II are *physically connected* to ribbons in Domain III, and their trends and geometries persist across domain boundaries (Figs. 9a and 9c). Therefore, if ribbons formed first in each of the domains, ribbons must be everywhere the first formed structures. Ribbon formation may have been spatially diachronous; however, the similarity of ribbons over the entire region and the coherence of the regional spatial pattern they describe are most easily explained if the ribbons formed broadly synchronously. Also, graben in all three domains postdate associated folds. Graben formation over the entire region could also be spatially diachronous, but is broadly the last phase of deformation. Thus the most likely sequence of deformation over the entire study area is (1) ribbons, (2) large folds, and (3) graben.

It is difficult to fit Domain I folds into this relative sequence, because Domain I lacks ribbons, large folds, and graben. Because the strain history for each domain strongly suggests that the BDT deepened with time over the entire region, it is reasonable that the structures reflecting the shallowest BDT (Domain I folds) formed early in the preserved deformation sequence. These folds occupy a small fraction of the plateau's area, and

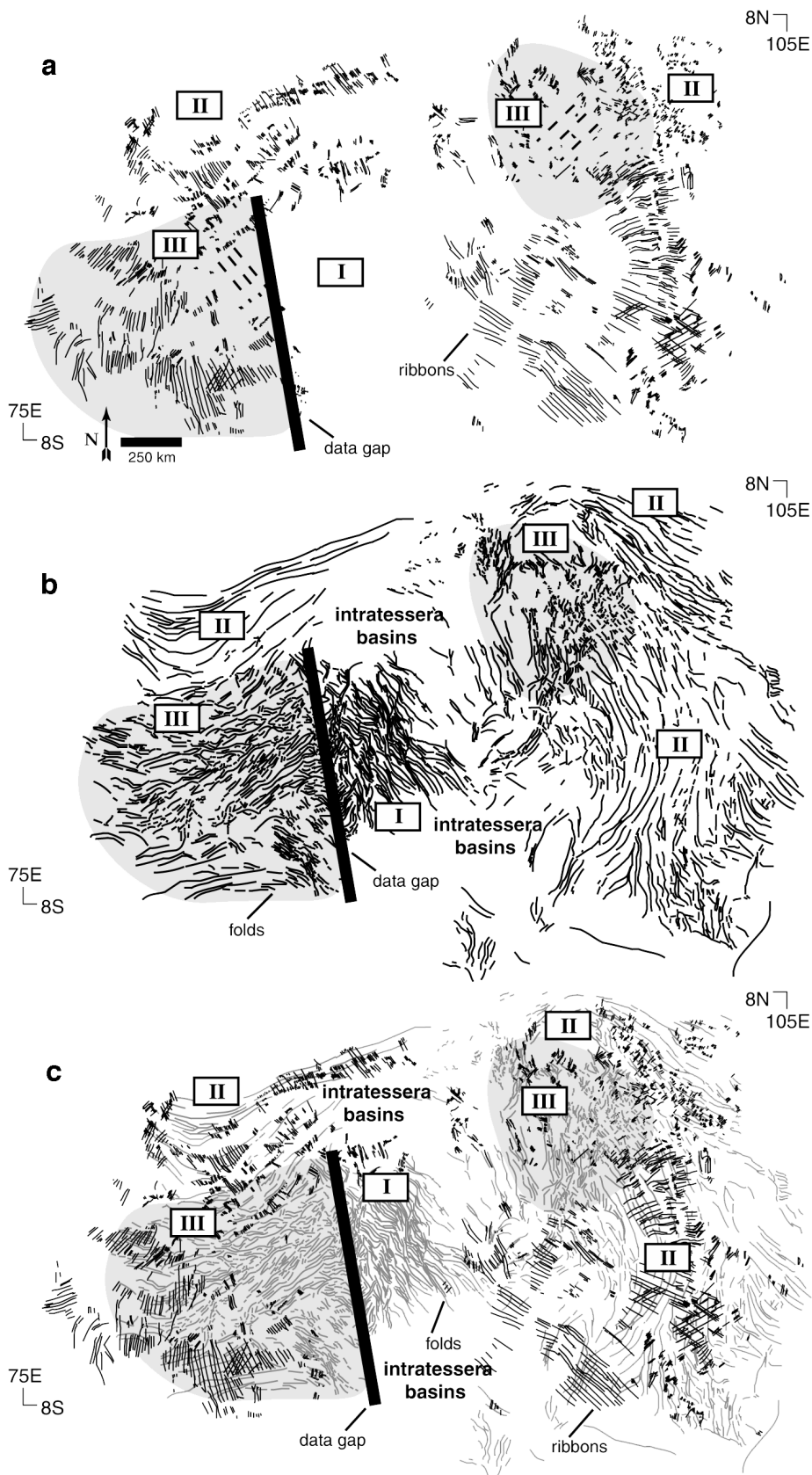


FIG. 9. Maps illustrating structural patterns across domain boundaries. Area same as Fig. 1. Shaded area denotes Domain III. (a) Ribbons mapped here are ~50% of the ribbons actually present. Note the broadly radial pattern over the study area and the coherence of ribbon orientations across domain boundaries. Ribbons are absent in Domain I. The dashed lines represent ribbon trends in Domain III; ribbons in these areas are too short, closely spaced, and narrow to be visible on this map. (b) Folds, which delineate domain boundaries. (c) Ribbons and folds together.

may therefore reflect local variations in stress or crustal properties at the time of their formation. The deformation Domain I folds record is not representative of the plateau as a whole.

Strain history. The structural data for all three domains comprise a coherent strain history for eastern Ovda, which reflects an early shallow BDT that deepened with time (Table III). The earliest recorded strain is radial membrane extension (ribbons), except in Domain I, which experienced interference folding of a thin layer, possibly in response to the surrounding thin-layer extension. The competent surface layer across the region thickened with time, and dominant strain changed from radial membrane extension to margin-parallel contraction at the plateau boundaries and interference folding in the plateau interior. The latest recorded strain is extension localized at fold crests.

The structures at any one location in the study area are consistent with a single bulk strain ellipse. There is no evidence for local reorientation of principal strain axes between phases of deformation. Furthermore, the orientations of local bulk strain ellipses define a coherent pattern relative to the plateau topography (Fig. 10). This implies that all three phases of deformation are intimately related and record stages of the same process. The result is a coherent and relatively simple preserved structural fabric. Reconnaissance mapping of other crustal plateaus and some large tessera inliers indicates that similar structural patterns and surface strain histories are preserved in those locations as well.

Dividing the strain history into three separate phases (early extension, intermediate contraction, and late extension) is a useful way to describe the process of deformation. However, any of these phases could be spatially diachronous or broadly synchronous. Our data place constraints on the relative timing be-

tween phases—for example, that ribbons most likely predated folds—but place no constraints on the absolute age or duration of deformation or on the time lapse between phases of deformation.

Craters and absolute timing? Impact craters on crustal plateau tessera have been used to infer the duration of folding in crustal plateaus (Gilmore *et al.* 1997). These workers argued that impact craters are deformed only by late graben; none are deformed by folds. They interpret this to indicate that folding occurred quickly. However, as outlined above, Ovda's folds generally represent $\ll 5\%$ shortening. A circular crater shortened by 5% would not appear greatly deformed, depending on the scale of the crater relative to the fold and where on the fold the crater is located. Gilmore *et al.* (1997) also stated that any craters which existed prior to crustal plateau deformation were eliminated by strong contractional deformation associated with tessera formation. Our analysis reveals no evidence for strong contractional deformation; and even 100% shortening (for which there is no evidence) would likely leave deformed but recognizable craters. Open folds (interlimb angles $>100^\circ$) accommodate the bulk of the contractional strain. Furthermore, the pristine character of preserved craters in Ovda are consistent with a lack of large-scale thrusting, at least expressed at the surface, unless all craters affected by thrust faults happened to be only in footwall locations and therefore completely covered; thus large-scale thrust faulting probably did not act to tectonically remove craters. Gilmore *et al.* (1997) also attempted to determine the absolute temporal duration of folding by binning all crustal plateau craters for statistical analysis. This binning assumes that all crustal plateau tessera is the same absolute age, yet there is no evidence to support this (see Hansen and Willis 1996). Furthermore, the small

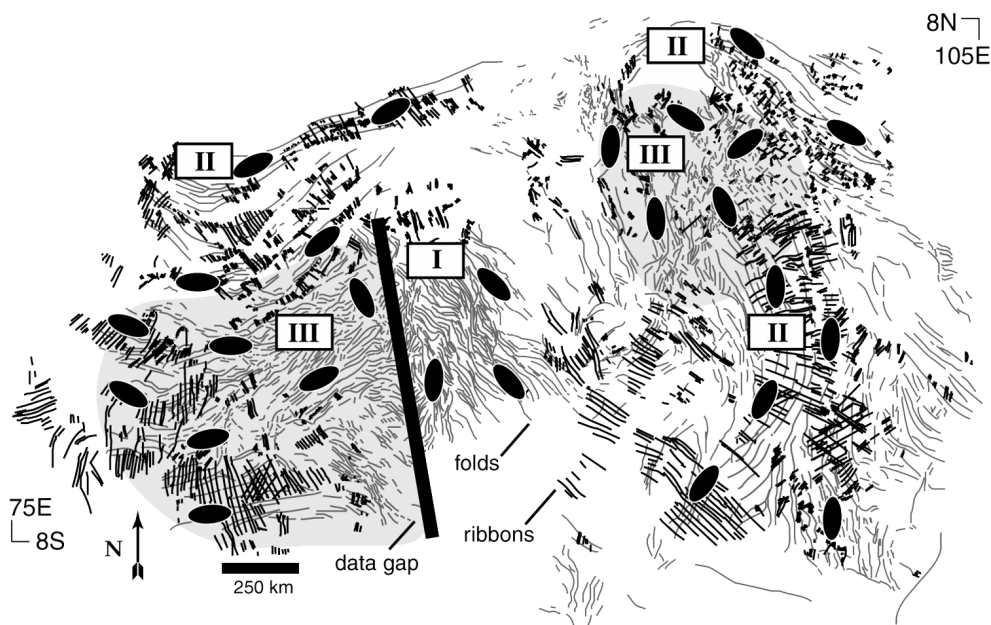


FIG. 10. Local strain ellipses superimposed on the structure map of Fig. 8. Strain ellipses, not drawn to scale, are intended to show the orientations of principal strain axes at various locations in the study area.

number of craters on Venus makes estimates of age based on crater density for any one class of terrain statistically meaningless (Campbell 1998). Thus our data and others' work contradict, or at best, fail to support, critical assumptions required by the analysis of Gilmore *et al.* (1997). We conclude that the crater record provides no constraints on the absolute age of surface deformation, nor on the duration of any phase of that deformation. Furthermore, Ovda's strain history indicates that at one time, the BDT was very close to (or at) the surface, indicating that the crust was ductile to very shallow levels; any impact craters present prior to the migration of the BDT to the surface would likely be annealed, and would leave no record of their existence (Hansen and Willis 1998).

SYNTHESIS

The goal of this work is to document the constraints on crustal plateau formation provided by preserved structures and other physical characteristics of Ovda Regio. Compiling the results of our structural analysis with characteristics of Ovda's gravity and topography, we arrive at the following. (a) Crustal plateaus show quasi-circular planforms with topography characterized by steep sides and approximately flat tops. (b) Ovda's gravity anomaly is spatially correlated with high topography (Bindschadler *et al.* 1992a), and indicates a shallow apparent depth of compensation interpreted to reflect support by thickened crust (Bindschadler and Parmentier 1990, Grimm 1994, Simons *et al.* 1997). Thus the steep topographic boundary suggests a sharp spatial transition from thin to thick crust at the plateau boundary. (c) Ovda's high topography is structurally bounded, and deformation is spatially correlative with topography. (d) Other crustal plateaus and some large tessera inliers preserve similar relationships between high topography and structural patterns as in Ovda Regio (Phillips and Hansen 1994, Hansen *et al.* 1997). (e) Ovda's surface records a strain history of regional extension by layer-normal flattening, followed by minor organized contraction at the plateau margins and constriction in the interior, and finally, local extension limited to fold crests. (f) The regional BDT was very shallow—possibly at the surface—early in Ovda's evolution and then deepened with time.

In order to use these constraints to evaluate models for crustal plateau formation, we must first ask the question: What is the global distribution of tessera terrain? Is it globally continuous, cropping out only in crustal plateaus, or is it localized to crustal plateaus? If tessera is globally distributed, we must conclude that crustal plateau deformation was not genetically related to crustal thickening and plateau uplift, because crustal plateaus and inliers are spatially localized. If tessera is instead localized to crustal plateaus, we may conclude either that surface deformation and crustal thickening processes were genetically related or unrelated. We can further conclude in this case that tessera formation must have occurred during or after plateau uplift; otherwise, the plateaus would have to have been serendipitously uplifted to coincide exactly with the preexisting deformation.

Several current resurfacing and geodynamic models rely on the global tessera hypothesis (e.g., Solomon 1993a,b, Turcotte 1993, Herrick 1994, Nimmo and McKenzie 1998). Proponents of this hypothesis (e.g., Ivanov and Head 1996, Head and Basilevsky 1998, Head and Coffin 1998) hold that regional plains lava generally embays tessera terrain (i.e., crustal plateaus and large inliers) and that other tectonic features deform these flows. This leads to a global "stratigraphic" sequence (encompassing both lithologic units and tectonic features), in which tessera terrain is a geologic unit residing at the base of a global stratigraphic column. These authors then conclude that because at some locations the regional plains slope away from the plains-tessera "contact," plains lava has embayed tessera terrain, and tessera therefore forms a global layer, locally uplifted in crustal plateaus and large inliers. This scenario cannot satisfy constraint (c), except by remarkable coincidence. We have demonstrated that tessera terrain preserved at Ovda Regio exhibits a well-defined structural pattern, the limits of which are defined by organized fold belts. Reconnaissance mapping shows this to be true in the other crustal plateaus and some tessera inliers, as well. If tessera formed a global layer, then we would have to conclude, based on exposed areas, that similar patterns persist everywhere under the plains. If this were the case, it would be remarkably fortuitous that uplift occurred such that at least four resulting quasi-circular plateau planforms (Ovda, Thetis, and Alpha regions and Tellus Tessera) coincided exactly with individual pattern units. Thus the best explanation for our observations is that tessera is not globally continuous, but is restricted to regions where it is currently preserved.

Another model for tessera formation spatially associates tessera with crustal plateaus, but divorces surface deformation from processes responsible for crustal thickening and plateau uplift (Solomon *et al.* 1998). In this model, excursions in surface temperature result from emission of magmatically derived greenhouse gases following one or more regional- or global-scale magmatic events. Prolonged periods of anomalously high surface temperature would lower the crustal viscosity of *already-high* plateaus supported by thickened crust, and allow thermal and gravitational stresses to create tessera terrain. This model predicts global synchronicity of tessera formation, but not global continuity; deformation is dependent on high topography, and should differ for areas of differing elevation. Constraint (d), then, would imply that all preserved crustal plateaus and large tessera inliers were at approximately the same elevation during the period of high surface temperature. Some, therefore, must have been uplifted or subsided since tessera formation. There is no structural evidence for this; all of the crustal plateaus and inliers show the same broad structural relationships as those recorded at Ovda Regio. Furthermore, this model does not explain the observed structural patterns; the ribbons, in particular, which should (in the Solomon *et al.* (1998) model) be gravitational collapse features, are oriented 90° to their predicted orientations relative to plateau topography and fold limbs, and their orientations are not apparently controlled by any local

topographic variations, but show incredible coherence over the whole plateau.

The constraints outlined above indicate instead that crustal plateau surface deformation was genetically related to crustal thickening and plateau uplift. Two current models might account for this relationship: the downwelling, or coldspot, model (e.g., Bindschadler and Parmentier 1990, Bindschadler and Head 1991, Bindschadler *et al.* 1992a,b, Bindschadler 1995) and the upwelling, or hotspot, model (Hansen and Willis 1998, Phillips and Hansen 1998). The downwelling model proposes that crustal plateaus formed above long-lived convective or diapiric mantle downwellings, resulting in horizontal convergence of ductile lower crustal material due to mechanical coupling between crust and mantle. The subsolidus flow of crustal material, if maintained long enough, would lead to crustal thickening. By contrast, the upwelling model proposes that crustal plateaus are large igneous provinces produced by mantle plumes impinging on thin lithosphere; crustal thickening occurs by magmatic processes. This upwelling model is distinct from the pre-Magellan upwelling models of Herrick and Phillips (1990) and Phillips *et al.* (1991), which have been discarded on the basis of Magellan observations (e.g., Bindschadler *et al.* 1992a, Phillips and Hansen 1994). We examine the downwelling and new upwelling models in light of each of the above constraints.

(a) Both the downwelling and upwelling models can accommodate quasi-circular planforms, if the proposed downwelling is axisymmetric. However, models of sustained axisymmetric mantle downwelling do not predict steep-sided, flat-topped plateau topography, but rather predict a broad swell or topographic dome (Bindschadler and Parmentier 1990, Fig. 13a; Kidder and Phillips 1996, Fig. 7). Upwelling, by contrast, can accommodate crustal plateau shape; even though the initial crustal response to the presence of a mantle plume would be a broad swell, magmatic accretion, and viscous relaxation following loss of thermal support would lead to steep sides and a flat top. Terrestrial oceanic plateaus, known to form by plume-type upwelling beneath relatively thin lithosphere, exhibit steep sides and flat tops.

(b) Both the downwelling and the upwelling models can accommodate the spatial correlation of gravity with topography. However, mantle downwelling does not result in a sharp transition from thin to thick crust at the plateau boundary, but produces a gentle shape mirroring the surface topographic swell (Bindschadler and Parmentier 1990, Fig. 13a; Kidder and Phillips 1996, Fig. 7). By contrast, the Hawaiian islands, formed over a terrestrial mantle plume, are underlain by magmatically thickened crust which transitions sharply to typically thin oceanic crust (Watts and tenBrink 1989, Fig. 15).

(c) Both the downwelling and the upwelling models can accommodate spatial correlation of structures with topography. In both cases, underlying mantle flow causing plateau formation is localized beneath the plateau; thus surface strain should be localized to the same region.

(d) Both the downwelling and the upwelling models can accommodate similarities among crustal plateaus and tessera inliers. In both models, these features each form by a similar mechanism, which links surface deformation to plateau uplift, but does not depend on the amount of uplift to produce the preserved structures. Furthermore, neither model places constraints on the age of any individual plateau or requires synchronicity of individual plateau formation. Both models allow viscous relaxation of thickened crust following cessation of mantle flow, which could lead to subsidence and “sinking” of old plateaus relative to young plateaus.

(e) The downwelling model predicts a strain history of early, intense contraction, followed by late extension resulting from gravitational relaxation (Bindschadler *et al.* 1992a). This is contrary to the above outlined strain history of extension–contraction–extension. Furthermore, the downwelling model calls for much more contractional strain than is actually recorded (e.g., Bindschadler *et al.* 1992a,b). In contrast, the upwelling model predicts early extension, followed by minor contraction and late local minor extension (Hansen and Willis 1998, Phillips and Hansen 1998).

(f) The downwelling model never allows for the BDT to approach the surface. Mantle downwelling would be expected to cause the BDT to deepen until a sufficiently thick accumulation of crustal material exposed to high mantle temperatures experienced partial melting. This melt would likely not migrate very far upward, bringing the BDT to the surface over the whole plateau, but would likely pond and crystallize in the subsurface. The upwelling model, however, predicts pervasive crustal fracturing upon plume–lithosphere contact, resulting in magmatic injection, intrusion, and extrusion, heating the crust to ductility, and likely producing lava flows at the surface (Phillips and Hansen 1998). Subsequent cooling from the surface downward would cause the BDT to deepen with time. Thus the upwelling model satisfies constraint (e), whereas the downwelling model does not.

A New Upwelling Model

The upwelling model of Phillips and Hansen (1998) is distinct from, and should not be confused with, pre-Magellan upwelling models, of which there were two: the spreading center model (Head and Crumpler 1987), in which crustal plateaus were thought to be sites of Earth-like crustal production; and the volcanic rise model (e.g., Herrick and Phillips 1990, Phillips *et al.* 1991), in which volcanic rises were proposed to evolve into crustal plateaus. The spreading center model was rejected because it does not accommodate the quasi-circular planforms of crustal plateaus, and Magellan SAR images showed no evidence for large-scale crustal production or the expected rift-like structures (e.g., Bindschadler *et al.* 1992a, Grimm 1994). Furthermore, Magellan gravity data indicate no thermal signature for crustal plateaus (e.g., Bindschadler *et al.* 1992a, Phillips and Hansen 1994, Simons *et al.* 1997). The volcanic rise model

was rejected because Magellan SAR images showed no evidence for large-scale constructional volcanism or related structures (Bindschadler *et al.* 1992a, Phillips and Hansen 1994, Bindschadler 1995). The new upwelling model (Phillips and Hansen 1998) derives from recent observations of Magellan SAR data (Hansen and Willis 1996, Pritchard *et al.* 1997, Hansen and Willis 1998), including those outlined here. In this new model, volcanic rises and crustal plateaus are both surface expressions of mantle plumes, but *at different times* in Venus' history, reflecting different tectonic regimes. Volcanic rises result from mantle plumes interacting with thick (~100 km) lithosphere in the modern stagnant lid convective environment (e.g., Phillips 1994, Moore and Schubert 1995, Phillips and Hansen 1998; see also Solomatov and Moresi 1996), at a surface temperature of ~750 K (Barsukov *et al.* 1992). Crustal plateaus resulted from mantle plumes interacting with thin lithosphere under an ancient mobile lid convective regime, possibly accompanied by a surface temperature as high as 1000 K (Phillips and Hansen 1998). High surface temperatures may have resulted from magmatic outgassing accompanying widespread regional plains volcanism due to pressure-release melting in the shallow mantle as a consequence of regionally or globally thin lithosphere. Plumes impinging on thin lithosphere in a high-temperature environment would likely bow and pervasively fracture the lithosphere, and magmatic processes such as injection into fractures, intrusion, extrusion of flows, and underplating would thicken the crust. During this process, the thin crust overlying the plume would become ductile by mixing with magma (Phillips and Hansen 1998, Hansen *et al.* 1998). At this point, the BDT would be at or near the surface; preexisting features such as impact craters would relax, leaving no record of their existence. Following the initial arrival of the plume head, but before the plume completely waned, the crust would begin to cool from the surface downward, causing the BDT to progressively deepen with time. Tensional stresses related to cooling and bowed topography would cause pervasive fracturing (ribbon formation) of the cooling and strengthening surface layer, underlain by hotter and therefore more ductile material. With further cooling and waning of thermal support, topography would subside and the dominant surface stresses would transition from tensional to compressional, leading to organized margin-parallel folding, further thickening the crust locally at the plateau margins. Subsidence in the plateau interior would lead to constriction and interference folding. Finally, gravitational relaxation at overthickened fold crests would lead to graben formation.

CONCLUSIONS

Our comprehensive structural and kinematic analysis of eastern Ovda leads to the following conclusions.

1. Structural patterns and correlations between deformation, topography, and gravity indicate that crustal thickening and surface deformation were genetically related at Ovda Regio. The

similarities among crustal plateaus and large tessera inliers suggests that this is the case for all of these features and that similar processes formed each of them individually.

2. The strain history recorded at Ovda Regio reflects pervasive regional extension, followed by minor regional contraction, then minor localized extension. This strain history is consistent with formation by an upwelling mantle plume impinging on thin lithosphere, and inconsistent with formation by localized mantle downwelling and horizontal lower crustal flow.

3. The structural patterns at Ovda Regio also indicate an early shallow BDT and a progressive increase in the depth to BDT with time. This constraint supports a mantle plume origin rather than a mantle downwelling origin for crustal plateaus.

4. The topographic and inferred subsurface shapes of crustal plateaus are also more consistent with the upwelling plume model than with the downwelling model.

Future work, focusing on the details of the plume–lithosphere interaction within the framework of this model will provide valuable constraints on the mechanisms of heat loss on Venus in the past, and thereby will help to elucidate the thermal and tectonic history of the planet.

ACKNOWLEDGMENTS

This work was supported by National Aeronautics and Space Administration Grant NAGW-2915 to VLH and by an Institute for the Study of Earth and Man at Southern Methodist University SEED grant to R.R.G. Discussions with Roger Phillips were helpful. Reviews by M. S. Gilmore, F. Bilotti, and C. D. Brown called our attention to areas which needed clarification and thus helped to improve the quality of the manuscript.

REFERENCES

- Banerdt, W. B., and M. P. Golombek 1988. Deformational models of rifting and folding on Venus. *J. Geophys. Res.* **93**, 4759–4772.
- Banerdt, W. B., and C. G. Sammis 1992. Small-scale fracture patterns on the volcanic plains of Venus. *J. Geophys. Res.* **97**, 16,149–16,166.
- Banks, B. K., and V. L. Hansen 1998. Crustal plateau intra-tessera flood lava basins, Venus: *Geol. Soc. Amer. Abstr. Progs.* **30**, A-190.
- Barsukov, V. L., A. T. Basilevsky, V. P. Volkov, and V. N. Zharkov 1992. *Venus Geology, Geochemistry, And Geophysics: Research Results From The USSR*. University of Arizona, Tucson, AZ.
- Barsukov, V. L., A. T. Basilevsky, G. A. Burba, N. N. Bobinna, V. P. Kryuchkov, R. O. Kuzmin, O. V. Nikolaeva, A. A. Pronin, L. B. Ronca, I. M. Chernaya, V. P. Shashkina, A. V. Garanin, E. R. Kushky, M. S. Markov, A. L. Sukhanov, V. A. Kotelnikov, O. N. Rzhiga, G. M. Petrov, Tu. N. Alexandrov, A. I. Sidorenko, A. F. Bogomolov, G. I. Skrypnik, M. Yu. Bergman, L. V. Kudrin, I. M. Dokshtein, M. A. Dronrod, P. A. Chochia, Yu. S. Tyuffin, S. A. Kadnichansky, and E. L. Akim 1986. The geology and geomorphology of the Venus surface as revealed by the radar images obtained by Veneras 15 and 16. *J. Geophys. Res.* **91**, D378–D398.
- Basilevsky, A. T., A. A. Pronin, L. B. Ronca, V. P. Kryuchkov, A. L. Sukhanov, and M. S. Markov 1986. Styles of tectonic deformation on Venus: Analysis of Venera 15 and 16 data. *J. Geophys. Res.* **91**, D399–D411.
- Bindschadler, D. L. 1995. Magellan: A new view of Venus' geology and geophysics. *Rev. Geophys. Suppl. US Natl. Rep. Int. Union Geodesy Geophys.* 459–467.
- Bindschadler, D. L., and J. W. Head 1991. Tessera terrain, Venus: Characterization and models for origin and evolution. *J. Geophys. Res.* **96**, 5889–5907.

- Bindschadler, D. L., and E. M. Parmentier 1990. Mantle flow tectonics: The influence of a ductile lower crust and implications for the formation of topographic uplands on Venus. *J. Geophys. Res.* **95**, 21,329–21,344.
- Bindschadler, D. L., A. DeCharon, K. K. Beratan, S. E. Smrekar, and J. W. Head 1992b. Magellan observations of Alpha Regio: Implications for formation of complex ridged terrains on Venus. *J. Geophys. Res.* **97**, 13,563–13,577.
- Bindschadler, D. L., G. Schubert, and W. M. Kaula 1992a. Coldspots and hotspots: Global tectonics and mantle dynamic of Venus. *J. Geophys. Res.* **97**, 13,495–13,532.
- Brown, C. D., and R. E. Grimm 1997. Tessera deformation and the contemporaneous thermal state of the plateau highlands, Venus. *Earth Planet. Sci. Lett.* **147**, 1–10.
- Bullock, M. A., and D. H. Grinspoon 1996. The stability of climate on Venus. *J. Geophys. Res.* **101**, 7521–7529.
- Campbell, B. A. 1998. Surface formation rates and impact crater densities on Venus. *J. Geophys. Res.*, in press.
- Connors, C. 1995. Determining heights and slopes of fault scarps and other surfaces on Venus using Magellan stereo radar. *J. Geophys. Res.* **100**, 14,361–14,381.
- Farr, T. G. 1993. Radar interactions with geologic surfaces. In *Guide to Magellan Image Interpretation* (J. P. Ford, J. J. Plaut, C. M. Wietz, T. G. Farr, D. A. Senske, E. R. Stofan, G. Michaels, and T. J. Parker, Eds.), pp. 45–56. NASA JPL, Pasadena.
- Ford, J. P., and J. J. Plaut 1993. Magellan image data. In *Guide to Magellan Image Interpretation* (J. P. Ford, J. J. Plaut, C. M. Wietz, T. G. Farr, D. A. Senske, E. R. Stofan, G. Michaels, and T. J. Parker, Eds.), pp. 7–18. NASA JPL, Pasadena, CA.
- Ford, J. P., R. G. Blom, J. A. Crisp, C. Elach, T. G. Farr, R. S. Saunders, E. E. Theiug, S. D. Wall, and S. B. Yewell 1989. *Spaceborne Radar Observations—A Guide for Magellan Radar-Image Analysis*. JPL, Pasadena, CA.
- Ghosh, S. K. 1988. Theory of chocolate tablet boudinage. *J. Struct. Geol.* **10**, 541–553.
- Gilmore, M. S., G. C. Collins, M. A. Ivanov, L. Marinangeli, and J. W. Head 1998. Style and sequence of extensional structures in tessera terrain, Venus. *J. Geophys. Res.* **103**, 16,813–16,840.
- Gilmore, M. S., M. A. Ivanov, J. W. Head, and A. T. Basilevsky 1997. Duration of tessera deformation on Venus. *J. Geophys. Res.* **102**, 13,357–13,368.
- Golombek, M. P. 1985. Fault type predictions from stress distributions on planetary surfaces: Importance of fault initiation depth. *J. Geophys. Res.* **90**, 3065–3074.
- Golombek, M. P., and W. B. Banerdt 1990. Constraints on the subsurface structure of Europa. *Icarus* **83**, 441–452.
- Grimm, R. E. 1994. The deep structure of venusian plateau highlands. *Icarus* **112**, 89–103.
- Grimm, R. E., and R. J. Phillips 1991. Gravity anomalies, compensation mechanisms, and the geodynamics of western Ishtar Terra, Venus. *J. Geophys. Res.* **96**, 8305–8324.
- Grimm, R. E., and R. J. Phillips 1992. Anatomy of a venusian hotspot: Geology, gravity, and mantle dynamics of Eistla Regio. *J. Geophys. Res.* **97**, 16,035–16,054.
- Hansen, V. L., and J. J. Willis 1996. Structural analysis of a sampling of Tesserae: Implications for Venus geodynamics. *Icarus* **123**, 296–312.
- Hansen, V. L., and J. J. Willis 1998. Ribbon terrain formation, southwestern Fortuna Tessera, Venus: Implications for lithosphere evolution. *Icarus* **132**, 321–343.
- Hansen, V. L., R. J. Phillips, J. J. Willis, and R. R. Ghent. Comment to Gilmore *et al.* (1998): Style and sequence of extensional structures in tessera terrain, Venus. *J. Geophys. Res.*, submitted.
- Hansen, V. L., and J. J. Willis, and W. B. Banerdt 1997. Tectonic overview and synthesis. In *Venus II* (S. W. Bougher, D. M. Hunten, and R. J. Phillips, Eds.), pp. 797–844. Univ. of Arizona Press, Tucson.
- Head, J. W. 1995. Tectonic facies in Venus tessera terrain: Clarification and interpretation of sequence of deformation. *Lunar Planet. Sci.* **26th**, 579–580.
- Head, J. W., and A. T. Basilevsky 1998. Sequence of tectonic deformation in the history of Venus: Evidence from global stratigraphic relationships. *Geology* **26**, 35–38.
- Head, J. W., and M. F. Coffin 1998. Large igneous provinces: A planetary perspective. In *Large Igneous Provinces: Continental, Oceanic, and Planetary Flood Volcanism*, American Geophysics Union Monograph 100, pp. 411–438.
- Head, J. W., and L. S. Crumpler 1987. Evidence for divergent plate-boundary characteristics and crustal spreading on Venus. *Science* **238**, 1380–1385.
- Herrick, R. R. 1994. Resurfacing history of Venus. *Geology* **22**, 703–706.
- Herrick, R. R., and R. J. Phillips 1990. Blob tectonics: A prediction for western Aphrodite Terra, Venus. *J. Geophys. Res.* **95**, 2129–2132.
- Hudleston, P. J., and L. Lan 1995. Rheological information from geological structures. *Pure Appl. Geophys.* **145**, 607–620.
- Ivanov, M. A., and J. W. Head 1996. Tessera terrain on Venus: A survey of the global distribution, characteristics, and relation to surrounding units from Magellan data. *J. Geophys. Res.* **101**, 14,861–14,908.
- Kaula, W. M. 1990. Venus: A contrast in evolution to Earth. *Science* **247**, 1191–1196.
- Keep, M., and V. L. Hansen 1994. The structural history of Maxwell Montes, Venus: Implications for venusian mountain belt formation. *J. Geophys. Res.* **99**, 26,015–26,028.
- Kidan, T. W., and J. W. Cosgrove 1996. The deformation of multilayers by layer-normal compression: An experimental investigation. *J. Struct. Geol.* **18**, 461–474.
- Kidder, J. G., and R. J. Phillips 1996. Convection-driven subsolidus crustal thickening on Venus. *J. Geophys. Res.* **101**, 23,181–23,294.
- Kobberger, G., and G. Zulauf 1995. Experimental folding and boudinage under pure constrictional conditions. *J. Struct. Geol.* **17**, 1055–1063.
- McGill, G. E. 1971. Attitude of fractures bounding straight and arcuate lunar rilles. *Icarus* **14**, 53–58.
- McGill, G. E., and A. W. Stromquist 1979. The grabens of Canyonlands National Park, Utah: Geometry, mechanics, and kinematics. *J. Geophys. Res.* **84**, 4547–4563.
- Moore, W. B., and G. Schubert 1995. Lithospheric thickness and mantle/lithosphere density contrast beneath Beta Regio, Venus. *Geophys. Res. Lett.* **22**, 429–432.
- Nimmo, W. F., and D. McKenzie 1998. Volcanism and tectonics on Venus. *Annu. Rev. Earth Planet. Sci.* **26**, 23–51.
- Phillips, R. J. 1990. Convection-driven tectonics on Venus. *J. Geophys. Res.* **95**, 1301–1316.
- Phillips, R. J. 1994. Estimating lithospheric properties at Atla Regio, Venus. *Icarus* **112**, 147–170.
- Phillips, R. J., and V. L. Hansen 1994. Tectonic and magmatic evolution of Venus. *Annu. Rev. Earth Planet. Sci.* **22**, 597–654.
- Phillips, R. J., and V. L. Hansen 1998. Geological evolution of Venus: A geodynamical and magmatic framework. *Science* **279**, 1492–1497.
- Phillips, R. J., R. E. Grimm, and M. C. Malin 1991. Hot-spot evolution and the global tectonics of Venus. *Science* **252**, 651–658.
- Plaut, J. J. 1993a. Stereo imaging. In *Guide to Magellan Image Interpretation* (J. P. Ford, J. J. Plaut, C. M. Wietz, T. G. Farr, D. A. Senske, E. R. Stofan, G. Michaels, and T. J. Parker, Eds.), pp. 33–43. NASA JPL, Pasadena, CA.
- Plaut, J. J. 1993b. The Non-SAR experiments. In *Guide to Magellan Image Interpretation* (J. P. Ford, J. J. Plaut, C. M. Wietz, T. G. Farr, D. A. Senske, E. R. Stofan, G. Michaels, and T. J. Parker, Eds.), pp. 19–31. NASA JPL, Pasadena, CA.

- Price, N. J., and J. W. Cosgrove 1990. *Analysis of Geological Structures*. Cambridge Univ. Press, Cambridge, England.
- Pritchard, M. E., V. L. Hansen, and J. J. Willis 1997. Structural evolution of western Fortuna Tessera, Venus. *Geophys. Res. Lett.* **24**, 2339–2342.
- Ramberg, H. 1955. Natural and experimental boudinage and pinch-and-swell structures. *J. Geol.* **63**, 512–526.
- Ramsay, J. G., and M. I. Huber 1983. *The Techniques of Modern Structural Geology: Strain Analysis*, Vol. 1. Academic Press, Oxford, England.
- Ramsay, J. G., and M. I. Huber 1987. *The Techniques of Modern Structural Geology: Folds and Fractures*, Vol. 2. Academic Press, Oxford, England.
- Rast, N. 1956. The origin and significance of boudinage. *Geol. Mag.* **93**, 401–408.
- Senske, D. A., and E. R. Stofan 1993. Geologic mapping on Venus. In *Guide to Magellan Image Interpretation* (J. P. Ford, J. J. Plaut, C. M. Weitz, T. G. Farr, D. A. Senske, E. R. Stofan, G. Michaels, and T. J. Parker, Eds.), pp. 135–140. NASA JPL, Pasadena, CA.
- Sherwin, J., and W. M. Chapple 1968. Wavelengths of single layer folds: A comparison between theory and observation. *Am. J. Sci.* **266**, 167–179.
- Simons, M., S. C. Solomon, and B. H. Hager 1997. Localization of gravity and topography: Constraints on the tectonics and mantle dynamics of Venus. *Geophys. J. Internat.* **131**, 24–44.
- Smith, R. B. 1977. Formation of folds, boudinage and mullions in non-Newtonian materials. *Geol. Soc. Am. Bull.* **88**, 312–320.
- Solomatov, V. S., and L.-N. Moresi 1996. Stagnant lid convection on Venus. *J. Geophys. Res.* **101**, 4737–4753.
- Solomon, S. C. 1993a. The geophysics of Venus. *Phys. Today* **46**, 48–55.
- Solomon, S. C. 1993b. A tectonic resurfacing model for Venus. *Lun. Planet. Sci.* **24th**, 1331–1332.
- Solomon, S. C., and J. W. Head 1984. Venus banded terrain: Tectonic models for band formation and their relationship to lithospheric thermal structure. *J. Geophys. Res.* **89**, 6885–6897.
- Solomon, S. C., M. A. Bullock, and D. H. Grinspoon 1998. Climate change as a regulator of global tectonics on Venus. *Lunar planet. Sci.* **29th**.
- Solomon, S. C., J. W. Head, W. M. Kaula, D. McKenzie, B. Parsons, R. J. Phillips, G. Schubert, and M. Talwani 1991. Venus tectonics: Initial analysis from Magellan. *Science* **252**, 297–312.
- Solomon, S. C., S. E. Smrekar, D. L. Bindschadler, R. E. Grimm, W. M. Kaula, G. E. McGill, R. J. Phillips, R. S. Saunders, G. Schubert, S. W. Squyres, and E. R. Stofan 1992. Venus tectonics: An overview of Magellan observations. *J. Geophys. Res.* **97**, 13199–13255.
- Stofan, E. R., D. A. Senske, and T. J. Parker 1993. Tectonic features in Magellan data. In *Guide to Magellan Image Interpretation* (J. P. Ford, J. J. Plaut, C. M. Weitz, T. G. Farr, D. A. Senske, E. R. Stofan, G. Michaels, and T. J. Parker, Eds.), pp. 93–108. NASA JPL, Pasadena, CA.
- Talbot, C. J. 1970. The minimum strain ellipsoid using deformed quartz veins. *Tectonophysics* **9**, 47–76.
- Tanaka, K. L., M. P. Golombek, and W. B. Banerdt 1991. Reconciliation of stress and structural histories of the Tharsis region of Mars. *J. Geophys. Res.* **96**, 15,617–15,633.
- Turcotte, D. L. 1993. An episodic hypothesis for venusian tectonics. *J. Geophys. Res.* **98**, 17,061–17,068.
- Twiss, R. J., and E. M. Moores 1992. *Structural Geology*. Freeman, New York.
- Watts, A. B., and ten Brink, U. S. 1989. Crustal structure, flexure, and subsidence history of the Hawaiian islands. *J. Geophys. Res.* **94**, 10,473–10,500.
- Weitz, C. M. 1993. Surface modification processes. In *Guide to Magellan Image Interpretation* (J. P. Ford, J. J. Plaut, C. M. Weitz, T. G. Farr, D. A. Senske, E. R. Stofan, G. Michaels, and T. J. Parker, Eds.), pp. 57–73. NASA JPL, Pasadena, CA.